Study of Cosmic Ray Background in the Balloon Experiment for the Gamma-ray Satellite GLAST (ガンマ線観測衛星 GLAST に向けた気球実験における宇宙線によるバックグラウンドの研究)

Hirofumi Mizushima
High-Energy Astrophysics and
Particle Physics (Experiment) Laboratory,
Department of Physical Science,
Graduate School of Science,
Hiroshima University

M1279026 水嶋 浩文
広島大学 理学研究科 物理科学専攻
高エネルギー宇宙・素粒子研究室

April 10, 2002

Abstract

The GLAST is a scientific satellite which observes gamma-ray universe and will be launched in 2006. The satellite is under development with an international cooperation of U.S.A, Japan, Italy, France, Germany and Sweden. The GLAST observes the whole universe with a highest sensitivity and is expected to advance a study of high energy phenomenon such as pulsars, active galactic nuclei and gamma-ray bursts.

To verify that the GLAST instruments works without problems in space-like high-radiation environment, and to record the cosmic-ray background events, a balloon experiment was performed in August 2001 at Palestine in Texas, U.S.A.. The Balloon Flight Engineering Model (BFEM) was developed for the experiment. The BFEM is composed of the tracker of silicon strip detector, calorimeter of CsI scintillator, anti coincidence detectors of plastic scintillator tiles and external gamma-ray targets of plastic scintillator blocks, and is equivalent to one sixteenth of the GLAST satellite. The balloon with the BFEM was launched successfully and entered into a level flight at an altitude of $\sim$38 km for about 3 hours. Cosmic-rays triggered in $\sim$500 Hz during the level flight, and more than 200,000 cosmic-ray events have been obtained by a telemetry system.

To achieve the high sensitivity required by the GLAST, we have to estimate the background produced by cosmic-rays precisely. As a first step of a development of a cosmic-ray models used in the GLAST background simulator, we have developed a Geant4-Based Monte-Carlo simulator for the GLAST balloon experiment, and constructed the detector geometry and cosmic-ray models.

We have run the simulator and compared the simulation results with the BFEM real data to develop reliable cosmic-ray models. We have compared the trigger rate and the Tracker hit information between them, and found that our simulator can reproduce the trigger rate within 15 % and the Tracker hit information well.

Contents

Chapter 1

Introduction

X-ray astronomy and gamma-ray astronomy started around 1970 by some pioneer missions, such as OSO-III (1967), COS-B (1975) and UHURU (1970). Some pulsars were identified in X- and gamma-rays, and diffuse gamma-ray emissions from the Milky Way was also discovered. Today, many astronomical sources, such as active galactic nuclei, black hole candidates, pulsars, super novae remnants, galaxies and clusters of galaxies are known to emit X- and gamma-rays. One of the important physical processes in these objects is a particle acceleration, and the gamma-ray observation with high sensitivity is essential to reveal the mechanism of these "natural accelerators".

A new era in the gamma-ray astronomy was opened by the EGRET, the Energetic Gamma-Ray Experiment Telescope onboard Compton Gamma-Ray Observatory (CGRO). During its life time from 1991 and 2000, it discovered many gamma-ray sources over 200 with its highest sensitivity ever achieved. The EGRET detected several gamma-ray pulsars and also established blazars as a class of extragalactic gamma-ray emitters. However, about half of the sources detected by the EGRET are unidentified since the angular resolution of the satellite was not sufficient to identify the sources. We also need to obtain energy spectrum of the gamma-ray sources with better quality to reveal their emission mechanism. In order to answer questions raised by the EGRET, understand the mechanism of particle acceleration, and discover new objects/phenomenon in gamma-ray astronomy, a new satellite called the Gamma-ray Large Area Space Telescope (GLAST) is planned to be launched in 2006. The main topic of this thesis is the balloon experiment for this satellite conducted in August, 2001.

Chapter 2

The GLAST satellite and Balloon Experiment

2.1 The GLAST satellite

The GLAST is a scientific satellite which observes gamma-rays from astronomical sources and will be launched in 2006. This is an international cooperation project of U.S.A, Japan, Italy, France, Germany and Sweden. The concept of the instruments and the satellite is shown in Figure 2.1. The main instrument of the GLAST, called Large Area Telescope (LAT), is made of 4×4 towers which is composed of the Tracker (TKR, silicon strip detector) and the Calorimeter (CAL, CsI scintillator). The towers are covered by plastic scintillators, called the Anti Coincidence Detector (ACD), to reject charged particle events. The TKR is composed of layer of silicon strip detectors (SSDs) and foils of high atomic number material as a gamma-ray converter. A gamma-ray which enters to instruments converts to a pair of electron and positron in the TKR. SSDs measure the tracks of these particles and a direction of a gamma-ray is determined from these tracks precisely and the CAL measures the energy. Energy range of the GLAST is from 20 MeV to 300 GeV. It has a wide field of view covering about 20 % of the enter sky, and effective area as large as $\sim$10000 cm^2. The performance of the GLAST and the EGRET operated from 1991 to 2000 is shown in Table 2.1, indicating that the GLAST will observe the gamma-ray universe with wide energy band, better energy resolution and much improved sensitivity. The GLAST surveys all sky with best sensitivity in its energy band.

The EGRET observed all sky in energy range from 20 MeV to 30 GeV, and proved that many active galactic nuclei and pulsars are gamma-ray emitters. Although it increased the number of gamma-ray objects over 200, most of them are unidentified as shown in Figure 2.2. The GLAST is expected to identify these sources with its high angular resolution.

2.2 The Balloon Experiment for the GLAST

The high energy photons from astronomical sources as well as cosmic-rays are stopped by the atmosphere and cannot reach the ground. This is why high energy gamma-ray observatory is needed to be outside the atmosphere like satellite orbit. However, instruments are also exposed to violent radiation of cosmic-rays at the satellite orbit, and the flux of these cosmic-rays overwhelms that of gamma-rays from astrophysical sources we

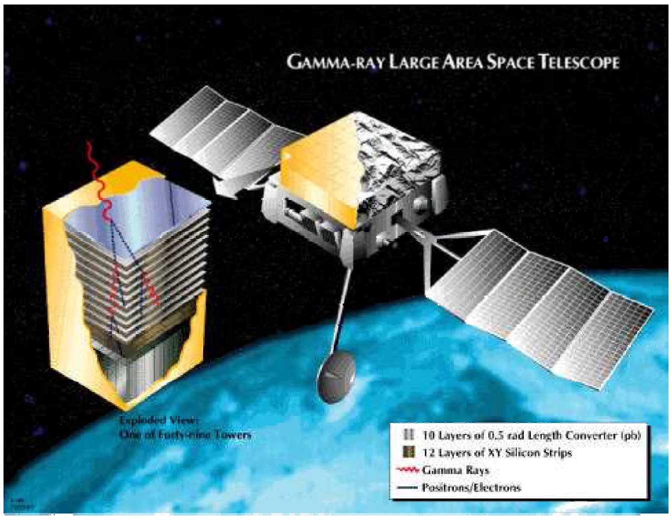

Figure 2.1: Schematic view of the GLAST satellite. A tower which consists of the Tracker and the Calorimeter is shown in left of the figure. The GLAST is composed of sixteen towers and the enveloping Anti Coincidence Detector.

are interested in. To verify that the GLAST instruments works without problems and to obtain cosmic-ray events used as background data base in space-like high-radiation environment, a balloon experiment was operated on August 4th, 2001 at Palestine in Texas, U.S.A.. This experiment also provided us with good opportunity to develop an efficient way of background rejection.

The Balloon Flight Engineering Model (BFEM) is developed for the balloon experiment based on the BeamTest Engineering Model (BTEM) used in the GLAST Beam Test 99 [1]. The photo of the real instruments is shown in Figure 2.3. The basic design of detectors is the same between the BFEM and the GLAST satellite. The TKR is composed of a pile of fourteen trays, and in a tray two layers of SSDs are placed on the top and bottom surface and a lead foil is placed between them as a gamma-ray converter. Plastic scintillator tiles called ACD are placed around the TKR. The CAL is placed under the TKR and is composed of eight layers in which ten logs of CsI scintillator are placed. Plastic scintillator blocks called eXternal Gamma-ray Targets (XGTs) are newly installed. When cosmic-ray particle hits the scintillator, induces inelastic scattering and π^0 mesons are generated, they immediately decay into gamma-rays. Therefore, we can obtain gamma-ray events of known position with XGTs. Data acquisition (DAQ) system

Quantity	EGRET	LAT (Minimum Spec.)
Energy Range	20 MeV – 30 GeV	20 MeV – 300 GeV
Peak Effective Area[1]	1500 cm^2	>8000 cm^2
Field of View	0.5 sr	>2 sr
Angular Resolution[2]	5.8° (100 MeV)	<3.5° (100 MeV) <0.15° (>10 GeV)
Energy Resolution[3]	10%	<10%
Deadtime per Event	100 ms	<100 μs
Source Location Determination[4]	15´	<0.5´
Point Source Sensitivity[5]	~1×10^{-7} cm^{-2} s^{-1}	<6×10^{-9} cm^{-2} s^{-1}

[1] After background rejection
[2] Single photon, 68% containment, on-axis
[3] 1-σ, on-axis
[4] 1-σ radius, flux 10^{-7} cm^{-2} s^{-1} (>100 MeV), high |*b*|
[5] >100 MeV, at high |*b*|, for exposure of one-year all sky survey, photon spectral index -2

Table 2.1: Performance of the GLAST LAT and the EGRET. The GLAST observes astronomical objects with larger effective area and field of view. Angular resolution and sensitivity of the GLAST is much improved than that of the EGRET.

was designed to operate even in high trigger rate expected in high-radiation environment and to send data to the ground by a telemetry during the flight as well as record them to hard disks. Instruments are covered by pressure vessel to keep inside to be a pressure of about 1.0 atmosphere.

The balloon with the BFEM was launched successfully and reached at an altitude of 38 km, 3.8 g/cm^2. The balloon stayed at the altitude for about three hours to the end of the flight, as shown in Figure 2.4. During an ascent the air in the pressure vessel began to leak and the pressure decreased to ∼0.14 atmosphere. At that time the DAQ system stopped to work and failed to remount hard disk and record data. However, detectors and trigger system kept to work correctly and the data sampled randomly was sent to the ground by the telemetry. The trigger rate was ∼500 Hz during the level flight and one of events is shown in Figure 2.5. The BFEM was confirmed to be able to treat events even in high-rate in space-like environment and the number of cosmic-ray events obtained by the telemetry is ∼ 200,000 in total.

The flux of gamma-ray from astronomical sources is much lower than that of cosmic-ray particles. Therefore, it is essential to estimate cosmic-ray background within 10 % accuracy with a simulation to accomplish high sensitivity required by the GLAST. To exploit cosmic-ray background models which can be used in the GLAST satellite simulator, a Monte-Carlo simulator for the GLAST balloon flight has been developed. The simulator is composed of mainly two parts, a detector geometry model and cosmic-ray background models. The geometry model of the BFEM is described in Chapter 3. The cosmic-ray background spectra are modeled based on measurement values (Chapter 4). We took into account the geomagnetic cutoff effect and solar modulation effect in the modeling, and they can be extended to be used in the GLAST satellite. We have ran the balloon flight simulator and compared the simulation results with the balloon experiment data, and tuned the simulator up based on comparative results to develop

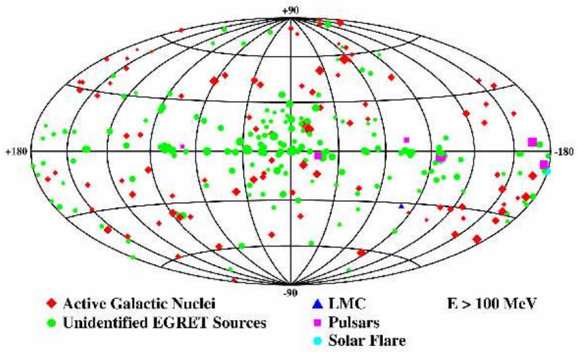

Figure 2.2: Third EGRET catalogue. The source location are shown in Galactic coordinates. The GLAST is expected to identify EGRET unknown sources by much better angular resolution.

reliable geometry and cosmic-ray models (Chapter 5).

Like the GLAST satellite, the Balloon experiment is an international collaboration project. Hiroshima university provided SSDs, XGTs and the simulator. The contents of this thesis is organized from two parts mainly. One is a development of the balloon experiment simulator (Chapter 3 and 4), and the other is a comparison of the balloon data with the simulation (Chapter 5).

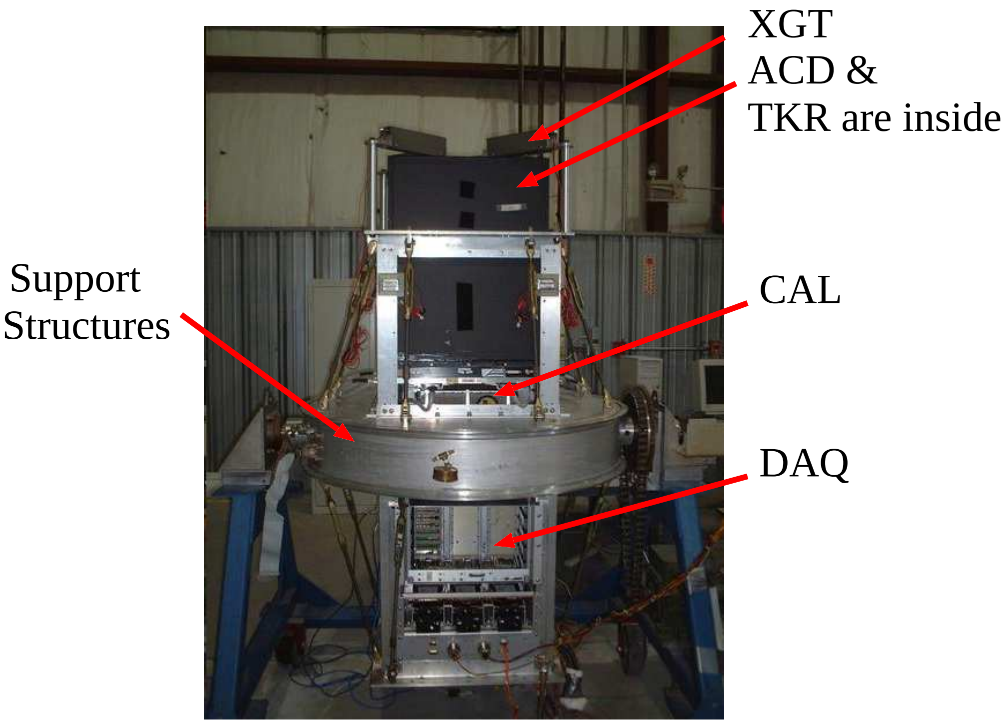

Figure 2.3: Balloon Flight Engineering Model (BFEM).

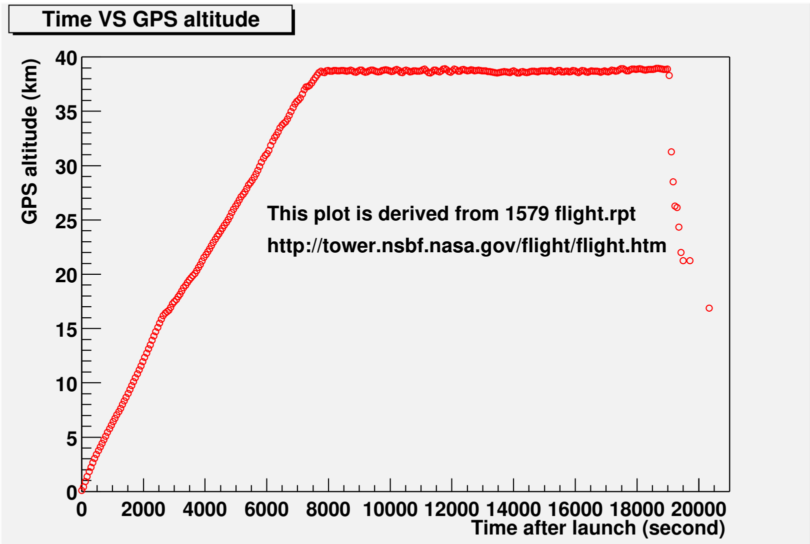

Figure 2.4: Time history of the altitude of the GLAST Balloon Flight. The altitude was measured by GPS system on board. The balloon went upward smoothly and reached at a floating altitude of 38 km. The level flight lasted for about three hours.

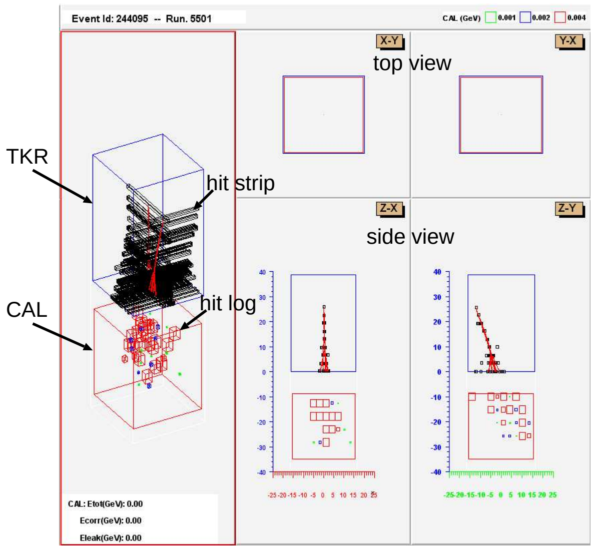

Figure 2.5: A sample of events during the level flight. Hit strips in the TKR and hit scintillator logs in the CAL are highlighted. ACDs and XGTs are not shown because they do not have hits.

Chapter 3

Development of the Balloon Flight Simulator

3.1 Overview of the Balloon Flight Simulator

In August 2001, we conducted the GLAST Balloon Experiment at Palestine, Texas and have obtained more than 200,000 cosmic-ray events to be used as background data base. We have developed a Geant4-based Monte-Carlo simulator, cosmic-ray background models and a detector geometry model, for the GLAST balloon flight to exploit cosmic-ray background models which can be used in a simulation at a satellite orbit. Geant4 is an object-oriented program for Monte-Carlo simulation of radiation passing through matter and provides base classes to build a detector geometry, generate primary radiations and so on. Users can construct a detector geometry and set any parts of detectors as “sensitive detector”, where we can obtain information of particle interaction. Users also can generate a primary particle of arbitrary type and momentum, and thus we can simulate the detector response for any radiation environment. We describe the detector geometry model and data format of the balloon flight simulator in this chapter and cosmic-ray models in Chapter 4.

3.2 Detector Geometry model in the Balloon Flight Simulator

3.2.1 Overview

The development of the geometry part in the GLAST balloon flight simulator was started by Hirano [2]. We tuned the program up and made that be closer to the real instruments. Scripts to convert Geant4 output to an “Instrument Response file” (IRF file, see § 3.4) are newly provided in May, 2001. In the simulator, we adapted the same coordinates system as that described in the Beam Test User’s Guide [3]. The center of the bottmmost silicon layer is defined to be (x, y, z) = (0, 0, 0), and z-direction is the CAL to the TKR. The principle axis of logs in the topmost CAL layer is the x-axis. The coordinate system as well as materials implemented in the simulator is shown in Figure 3.1. The TKR is composed of a pile of fourteen trays which have several materials including layers of Silicon Strip Detectors (SSDs) and lead converter foils. A gamma-ray entering into the TKR will be

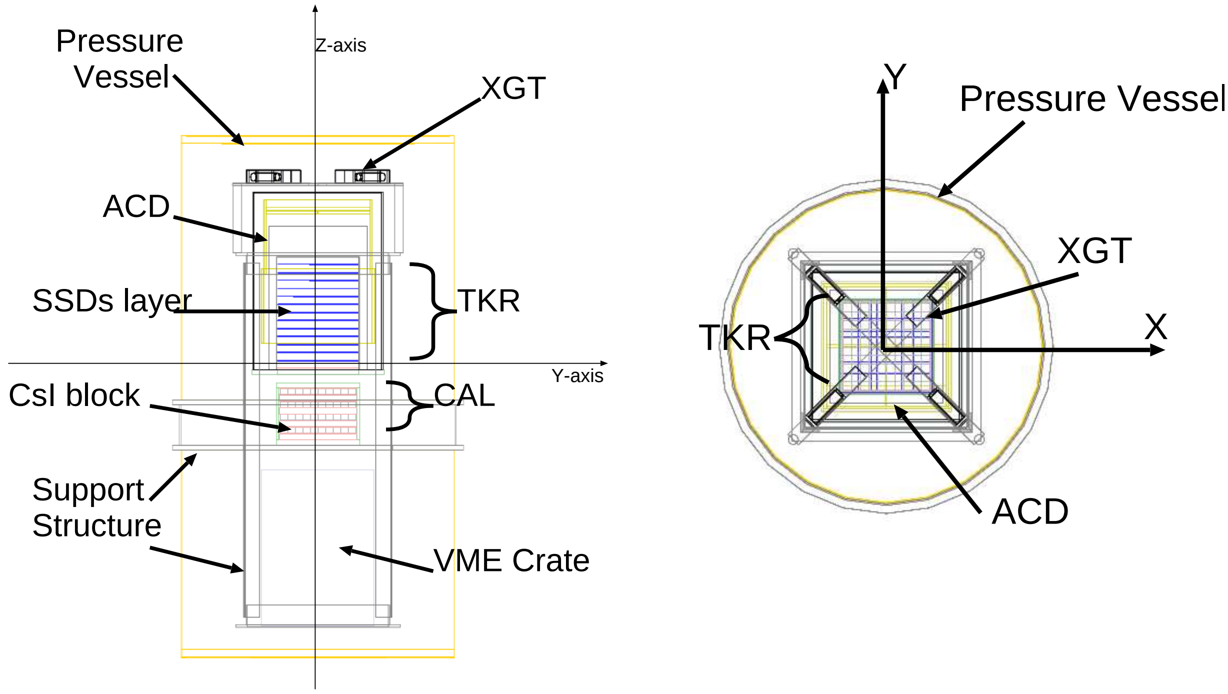

Figure 3.1: Geometry of the Balloon Flight Simulator. XGTs, TKR, CAL, ACD, VME crate, support structure and pressure vessel are implemented.

converted into a pair of electron and positron. The tracks of these particles are measured by SSDs layers precisely. We can determine the incident direction of gamma-ray by reconstructing tracks of these particles. The CAL made of CsI scintillators are placed under the TKR to measure the gamma-ray energy. Plastic scintillator tiles called the ACD are surrounding the TKR to reject charged particle events. Four plastic scintillator blocks with Photo Multiplier Tubes (PMT), called eXternal Gamma-ray Targets (XGTs), are newly installed for the balloon flight. When cosmic-ray particle hits the scintillator, inelastic scattering occurs and π^0 mesons are generated. They immediately decay into gamma-rays. Therefore, we can obtain gamma-ray events of known position and time with XGTs. In order to minimize the potential problems in the vacuum for the detector and electronics, the instruments are housed in a pressure vessel which keeps the internal pressure of $\sim$1.0 atmosphere.

3.2.2 Tracker (TKR)

The structure of one tray (a standard tray; see below) is shown in Figure 3.2. In the tray, two layers of SSDs are placed on top and bottom and lead converter layer lies between these two layers. Each tray is arranged alternatively in two perpendicular directions so that the bottom SSDs layer of one tray and the top one of the next tray work as x and y planes. There are eight trays from the top of the TKR with 3.6% radiation length converters

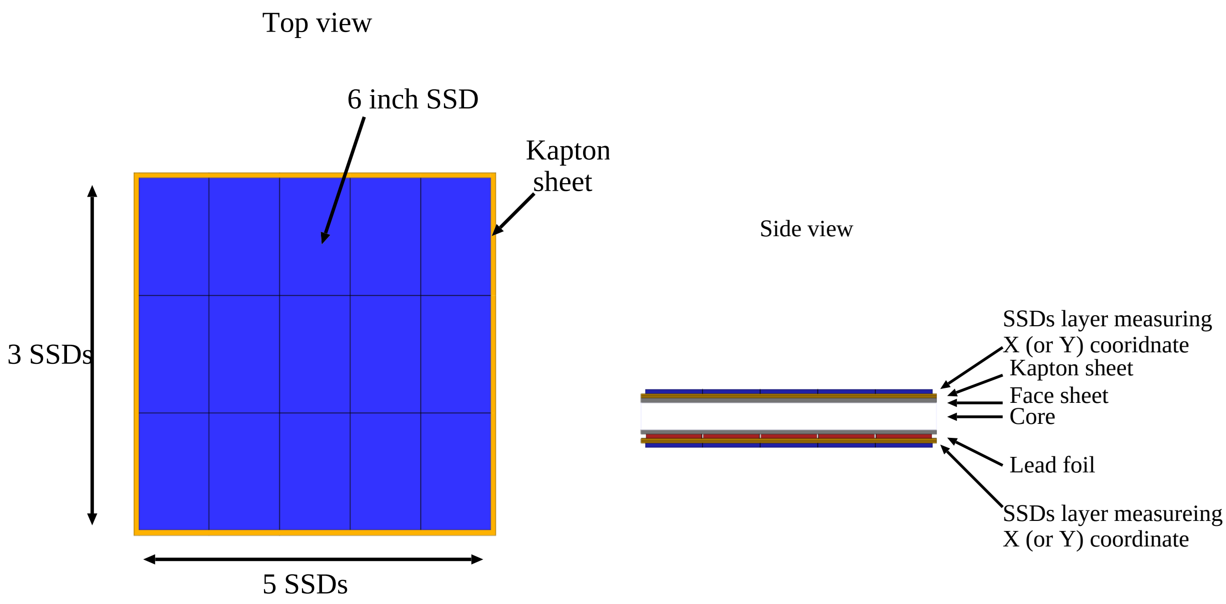

Figure 3.2: Schematic view of a standard tray. Top and side view are shown in left and right panel, respectively.

("standard trays" or "front section"), followed by three trays with 28% radiation length converters ("super GLAST trays" or "back section") and three trays with no converter foils ("no lead tray"), as shown in Figure 3.3. Components of each trays are summarized in Table 3.1. We neglect the readout electronics in the simulator for simplicity. SSDs wafers of different size called 4-inch ($64 \times 64 \times 0.395$ mm^3) or 6-inch ($64 \times 106.8 \times 0.395$ mm^3) wafer are used for the BFEM. Among 26 layers, 10 are not fully equipped with SSDs and we call them "incomplete layer". The number and the size of SSDs in each tray are shown in Table 3.2, and the size and material of components are summarized in Table 3.3. The ID numbers of each SSD layer is also shown in Table 3.2. Lead converters are placed so that the X and Y coordinate of the center is the same as those of SSDs. Although a "Core" is composed of aluminum honeycomb structure, we constructed it as an uniform aluminum box with a density of 0.016 g cm^{-3}, 0.6% of normal aluminum. We constructed kapton sheets by copper and polyamide sheet based on the information from the TKR team ("TRK2000_003.doc" (2000) [4]). There are some other materials around the TKR. Aluminum side walls surround the TKR, an aluminum stand is put under the TKR, and light shield box covers the whole TKR and ACDs. These materials are also included in the simulator. Elemental composition, size, and position of aluminum walls and stand are shown in Table 3.4. Carbon wall is described in § 3.2.3.

3.2.3 Carbon Wall

The light shield box surrounding the TKR and ACD is called as "Carbon Wall", since this wall is made of low density carbon. Dimension of the side wall is $520 \times 520 \times 711.209$ mm^3 and the thickness is 5.0 mm. The top wall is a box of $510 \times 510 \times 5.0$ mm^3, and

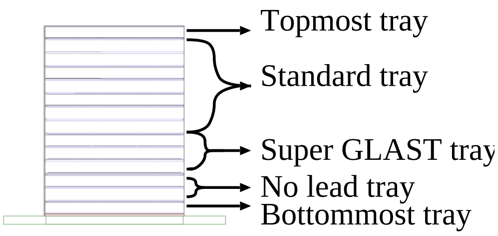

Figure 3.3: Schematic view of TKR, composed of 14 trays. Among them, eight trays are equipped with thin lead converter (standard tray) and three are with thick converter (Super GLAST tray). The bottommost three are without lead and called "no lead tray".

the center of this wall is (0, 0, 674.409 mm). The surface density of the wall is 0.15 g cm^{-2} (the information from the ACD team), or $\frac{0.15 \text{ g cm}^{-2}}{5 \text{ mm}} = 0.30$ g cm^{-3}.

3.2.4 Calorimeter (CAL)

The CAL is composed of eight layers in which ten logs of CsI scintillator are placed. The size and density of CsI log are $310.5 \times 30.0 \times 23.0$ mm^3 and 4.53 g/cm^3, respectively. Each layer is arranged alternatively in two perpendicular direction in order to get two-dimensional position information. Signals are read from both sides of a log, and a hit position in a log can be measured by the ratio of these signals. We also implemented support materials, i.e., polystyrene wrapping, rubber and aluminum sheets between layers and an aluminum frame. There are three kinds of ID numbers for the CAL, i.e., LayerID, LogID and LogDID. LayerID is numbered from 0 to 7 in increasing order with decreasing Z. LogID is numbered from 0 to 79 in increasing order with decreasing Z and increasing X or Y. In the simulator, one CsI log is divided into 10 virtual blocks to record a position where a particle goes through in a CsI log. These blocks are represented by LogDID numbered from 0 to 9 increasing order with increasing X or Y coordinate. The structure and ID numbering of the CAL are shown in Figure 3.4. The size and composition of materials are summarized in Table 3.5.

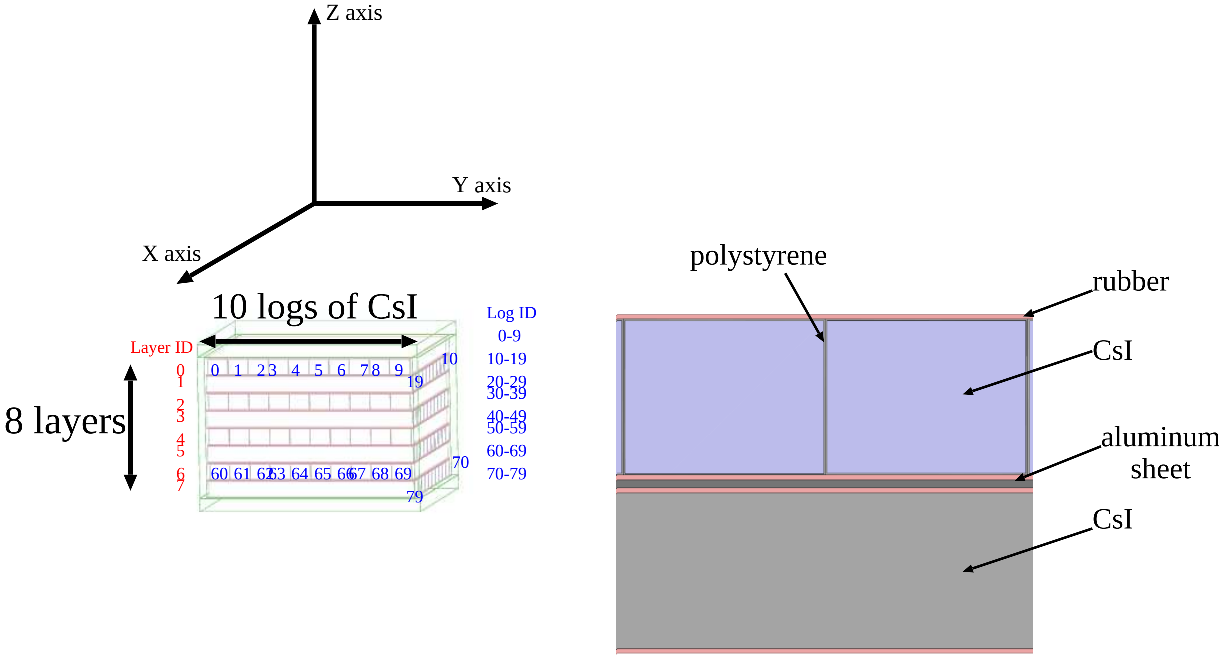

Figure 3.4: Schematic view of the CAL. A left panel is a overview of the CAL and ID numbering with coordinate system. A right one is an expanded view to show wrapping material configuration.

Table 3.1: Materials in each tray. The topmost tray is a Standard tray without upper Kapton and top SSD, and the bottommost tray is a No Lead tray without lower Kapton and bottom SSD.

	Bottommost Tray	No Lead Tray	Super GLAST Tray	Standard Tray	Topmost Tray
top SSD layer	◯	◯	◯	◯	—
Kapton sheet	◯	◯	◯	◯	—
Face sheet	◯	◯	◯	◯	◯
Core	◯	◯	◯	◯	◯
SuperGLAST Lead	—	—	◯	—	—
Face sheet	◯	◯	◯	◯	◯
Lead	—	—	—	◯	◯
Kapton sheet	—	◯	◯	◯	◯
SSD layer	—	◯	◯	◯	◯
Bottom	◯	—	—	—	—

3.2.5 Anti Coincidence Detector (ACD)

Four plastic scintillator tiles are placed above the TKR to cover the top of it and gap of these tiles are covered by one big tile above them. An each side of TKR is covered by two tiles placed lengthways, thus there are four upper side tiles and four lower ones in total. The thickness of each tiles are 10.0 mm and they are made of C_8H_8 of 1.032 g/cm^3. The size, position and ID numbers of ACD tiles are summarized in Table 3.6. For historical reason, ID numbering starts from two and jumps several times.

3.2.6 External Gamma-ray Target (XGT)

We implemented XGT scintillators and PMTs in our simulator. The scintillators are $5 \times 5 \times 10$ cm^3 blocks made of polystylen (C_8H_8) and placed 3.5 cm above the carbon wall. We implemented PMT assembly as nickel tube, because a magnetic shield metal is a main component. The dimension of the shield is 0.5 mm thickness, 33 mm diameter and 140 mm height. Then, the total mass of the tube is about 250 g, almost the same as that of PMT assembly. PMT is supported by acrylic boards and covered by an aluminum tube. The schematic view of PMT assembly and scintillator is shown in Figure 3.5. The size and composition of these materials of XGTs are summarized in Table 3.7, and positions of scintillator center and ID numbers are given in Table 3.8.

3.2.7 Pressure Vessel, VME Crate and Support Structure

Based on the drawings of the pressure vessel (http://www.slac.stanford.edu/~godfrey/Balloon_pv_9-27-00.tif), we implemented both upper dome and lower one of the vessel. We modeled each of them as an aluminum tube and a cover (consists of tube and plate) as shown in Figure 3.1. Parameters of these components are summarized in Table 3.9. We expressed

Table 3.2: Tray configuration. Ladders are loaded with five small SSDs (4 inch) or three large SSDs (6 inch). The number of ladders in each tray is listed. ID numbers of SSD are also listed with the coordinate that can be measured in brackets.

Tray	Top ladders				Bottom ladders				Lead
	No. of 4 in SSD	No. of 6 in SSD	Si ID	z (mm)	No. of 4 in SSD	No. of 6 in SSD	Si ID	z (mm)	radiation length (%)
14					3		25 (x)	387.908	3.6
13	2	1	24 (y)	387.792	3		23 (y)	355.842	3.6
12	3		22 (x)	352.726	3		21 (x)	323.776	3.6
11	3		20 (y)	320.66	3		19 (y)	291.71	3.6
10	3		18 (x)	288.594	4		17 (x)	259.644	3.6
9		4	16 (y)	256.528	5		15 (y)	227.578	3.6
8		5	14 (x)	224.462		5	13 (x)	195.512	3.6
7		5	12 (y)	192.396		5	11 (y)	163.446	3.6
6		5	10 (x)	160.33		5	9 (x)	131.58	28
5		5	8 (y)	128.264		5	7 (y)	99.514	28
4		5	6 (x)	96.198		5	5 (x)	67.448	28
3		5	4 (y)	64.132		5	3 (y)	35.382	0
2		5	2 (x)	32.066		5	1 (x)	3.316	0
1		5	0 (y)	0					0

a VME Crate in Geant4 simulator. Instead of modeling a detailed structure of VME electronics, we simply constructed aluminum of 130 kg with a box. The size and material are also summarized in Table 3.9. Instruments are supported by aluminum structures, as shown in Figure 3.1. Aluminum bars, poles and plates surround the Carbon Wall and "X"-shaped structure that supports XGTs is mounted on top of them. We implemented these support structures in our simulator. The dimensions of each structure are also summarized in Table 3.9.

Table 3.3: Material list of the TKR

material	elemental composition	density [g/cm^3]	size
4-inch Silicon	Si	2.330	$64.0 \times 64.0 \times 0.400$ mm^3
6-inch Silicon	Si	2.330	$64.0 \times 106.8 \times 0.400$ mm^3
4-inch Lead	Pb	11.35	$62.4 \times 62.4 \times 0.20$ mm^3
6-inch Lead	Pb	11.35	$62.4 \times 105.2 \times 0.20$ mm^3
Lead for super GLAST	Pb	11.35	$62.4 \times 105.2 \times 1.6$ mm^3
Core	Al	0.016	$330.2 \times 330.2 \times 27.9$ mm^3
Core for super GLAST	Al	0.016	$330.2 \times 330.2 \times 26.3$ mm^3
Polyamide of Kapton sheet	$C_{22}H_{10}O_5N_2$	1.420	$330.2 \times 330.2 \times 0.12$ mm^3
Cu of Kapton sheet	Cu	3.54	$330.2 \times 330.2 \times 0.029$ mm^3
Face sheet	C	1.467	$330.2 \times 330.2 \times 0.075$ mm^3
Bottom	Al	2.70	$330.2 \times 330.2 \times 5.5$ mm^3

Table 3.4: Materials used in Al wall and stand

material	elemental composition	density [g/cm^3]	size	z coordinate of the center (mm)
side wall	Al	2.70	$330.2 \times 1.5 \times 711.209$ mm^3	321.3045
stand	Al	2.70	$528.32 \times 528.32 \times 19.1$ mm^3 with 326.7×326.7 mm^2 hole	-43.85

Table 3.5: Material list of the CAL

Material	elemental composition	density [g/cm^3]	size
Scintillator	CsI	4.53	$310.5 \times 30.0 \times 23.0$ mm^3
Polystyrene	C_8H_8	1.032	0.25 mm thickness, wrapping CsI
rubber sheet	C_4H_6	1.00	$310.5 \times 310.5 \times 0.71$ mm^3
Al sheet	Al	2.700	$310.5 \times 310.5 \times 1.22$ mm^3
Frame (top)	Al	0.405	$332.13 \times 332.13 \times 20.0$ mm^3
(side)	Al	0.90	$332.13 \times 332.13 \times 310.2$ mm^3, 9.0 mm thickness
(bottom)	Al	2.700	$332.13 \times 332.13 \times 20.0$ mm^3

Table 3.6: The size and position of ACD tiles, they are made of C_8H_8 and have 10mm thickness.

size (mm)	position of tile center (mm)	ID number
300 (x) × 414 (y)	(12.0, 0.0, 610.7)	13
201 (x) × 205 (y)	(106.5, 104.5, 595.7)	20
201 (x) × 205 (y)	(-106.5, 104.5, 595.7)	21
201 (x) × 205 (y)	(-106.5, -104.5, 595.7)	15
201 (x) × 205 (y)	(106.5, -104.5, 595.7)	14
422 (y) × 300 (z)	(212.0, 4.0, 495.7)	8
422 (x) × 300 (z)	(-4.0, 212.0, 495.7)	7
422 (y) × 300 (z)	(-212.0, -4.0, 495.7)	9
422 (x) × 300 (z)	(4.0, -212.0, 495.7)	10
444 (y) × 300 (z)	(222.0, 5.0, 220.7)	2
444 (x) × 300 (z)	(5.0, -222.0, 220.7)	4
444 (y) × 300 (z)	(-222.0, -5.0, 220.7)	3
444 (y) × 300 (z)	(-5.0, 222.0, 220.7)	19

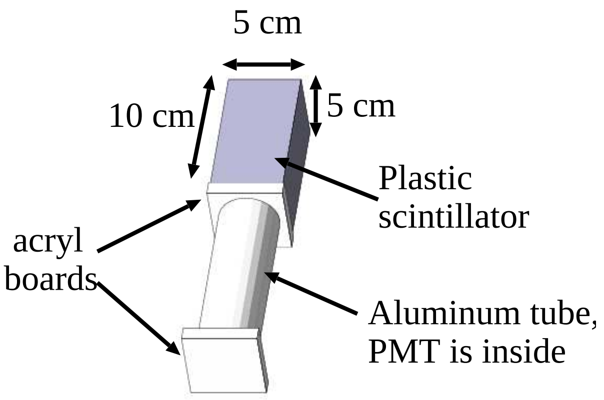

Figure 3.5: A schematic view of XGT.

Table 3.7: Material list of the XGT.

Material	elemental composition	density [g/cm^3]	size
Scintillator	C_8H_8	1.032	50 × 50 × 100 mm^3
PMT	Ni	8.85	1.625 mm/1.65 mm (inner/outer radius), length of 140 mm
Acrylic support	$C_5H_8O_2$	1.1	52 × 52 × 10 mm^3. 52 × 52 × 10 mm^3 with hole of 18 mm radius and 10 mm thickness.
Al support of the PMT	Al	2.7	18 mm/21 mm (inner/outer radius), length of 130 mm
Al cover of the scintillator	Al	2.7	255 × 52 × 1.0 mm^3 (side) 255 × 54 × 1.0 mm^3 (top)

Table 3.8: The center position and ID number of XGT scintillators.

position of XGT scintillator center (mm)	ID number
(123.74, 123.74, 737.909)	0
(123.74, -123.74, 737.909)	1
(-123.74, -123.74, 737.909)	2
(-123.74, 123.74, 737.909)	3

Table 3.9: Material and size of Pressure vessel, VME Crate and Support Structure.

Material	elemental composition	density [g cm^{-3}]	size
		Pressure Vessel	
upper Vessel (tube)	Al	2.70	544.5 mm (inner radius) 2.5 mm (thickness) 1028.00 mm (height)
lower Vessel (tube)	Al	2.70	544.5 mm (inner radius) 2.5 mm (thickness) 800.00 mm (height)
cover (tube)	Al	2.70	544.5 mm (inner radius) 2.5 mm (thickness) 30.00 mm (height)
cover (plate)	Al	2.70	547.0 mm (radius) 1.5/2.5 mm (thickness of top/bottom)
		VME Crate	
VME Crate	Al	1.02	450.850 $\times$ 450.850 $\times$ 627.016 mm^3
		Support Structure	
L-shape bar	Al	2.70	64 $\times$ 1421 $\times$ 6 mm^3 and 58 $\times$ 1421 $\times$ 6 mm^3
cylinder (plate)	Al	2.70	58.2 cm (radius) 1.905 mm (thickness) with 59.7 mm $\times$ 59.7 mm $\times$ 1.905 mm^3 hole
(middle cylinder)	Al	2.70	554 mm (radius), 5mm (thickness) 161.9 mm (height)
rectangular parallelepiped (plane)	Al	2.70	660 $\times$ 660 $\times$ 10 mm^3 with 575 $\times$ 575 $\times$ 10 mm^3 hole
(box)			575 $\times$ 575 $\times$ 77 mm^3 10 mm (thickness)
X-shape structure	Al	2.70	916 $\times$ 51 $\times$ 9 mm^3 another one cross at a right angle at the center
pole	Al	2.70	17 mm (radius) 270 mm (height)

3.3 Data Format of the Geant4 Outputs

Outputs of the Geant4 simulator are given in four ASCII files, "AntiOut.dat" (output of the ACD), "CalOut.dat" (output of the CAL), "TrackerOut.dat" (output of the TKR) and "TargetOut.dat" (output of the XGT). These are described in the following sections. All linear dimensions are written in unit of "mm" and all energy values are in "MeV".

3.3.1 ACD

A sample of "AntiOut.dat", output of ACDs, is shown in Figure 3.6. Event number is printed out at the beginning of each event in "EventNo=" and starts from 1. Information of a generated cosmic-ray particle is shown in the next two lines. A particle type and mass of a cosmic-ray is shown in "BEAM=" and "Mass=" in unit of MeV/c^2, and initial momentum and position are given in "PXYZ=" in unit of MeV/c and "XYZi=" (mm), respectively. "NoAntiHit=" is the number of hit tiles in each event. The ID number of hit tile and total deposit energy in the tile is printed out as "ID=" and "DepE=".

```
EventNo= 1
 BEAM= proton Mass= 938.272
  PXYZ= -7013.11 -16700.4 -3379.47 XYZi= 526.583 1803.74 908.729
 NoAntiHit= 2
  ID= 7    DepE= 3.47115
  ID= 9    DepE= 5.96276
EventNo= 14
 BEAM= proton Mass= 938.272
  PXYZ= -194.629 -147.325 224.795 XYZi= 1236.62 1307.58 -1208.18
 NoAntiHit= 2
  ID= 7    DepE= 44.2885
  ID= 19    DepE= 0.0392631
EventNo= 56
 BEAM= proton Mass= 938.272
  PXYZ= -5290.83 7987.87 -311.082 XYZi= 977.078 -1770.95 260.268
 NoAntiHit= 2
  ID= 3    DepE= 3.81576
  ID= 4    DepE= 2.15291
  ....
```

Figure 3.6: A part of AntiOut.dat.

3.3.2 XGTs

A samples of "TargetOut.dat", output of XGTs, is shown in Figure 3.7. Event number and incident cosmic-ray information is also shown in this output. The format of this file is quite similar to that of AntiOut.dat. "NoTargetHit=" is the number of hit scintillators in an event. The ID number of hit scintillator and total deposit energy in it are shown in "ID=" and "DepE=", respectively.

```
EventNo= 1
 BEAM= proton Mass= 938.272
  PXYZ= -7013.11 -16700.4 -3379.47 XYZi= 526.583 1803.74 908.729
 NoTargetHit= 1
  ID= 0    DepE= 15.7066
EventNo= 14
 BEAM= proton Mass= 938.272
  PXYZ= -194.629 -147.325 224.795 XYZi= 1236.62 1307.58 -1208.18
 NoTargetHit= 1
  ID= 1    DepE= 4.33581
EventNo= 56
 BEAM= proton Mass= 938.272
  PXYZ= -5290.83 7987.87 -311.082 XYZi= 977.078 -1770.95 260.268
 NoTargetHit= 0
  ....
```

Figure 3.7: A part of TargetOut.dat.

3.3.3 CAL

A sample of "CalOut.dat", output of the CAL, is shown in Figure 3.8. As described in previous section, event number is printed at the beginning of each event and informations of a cosmic-ray particle is shown in the following two lines. As we have explained in §3.2.4, the CAL consists of 80 logs and each log is divided into 10 blocks in the simulator. "NoCalHit=" is a number of hit blocks in a event. Position of a hit is represented by ID numbers of hit log, i.e., "LogDID=", "LogID=", and "LayerID=" (§3.2.4), and deposit energy is shown by "DepE=".

```
EventNo= 1
 BEAM= proton Mass= 938.272
  PXYZ= -7013.11 -16700.4 -3379.47 XYZi= 526.583 1803.74 908.729
 NoCalHit= 2
  LogDID= 7 LogID= 9 LayerID= 0  DepE= 55.8073
  LogDID= 6 LogID= 9 LayerID= 0  DepE= 22.7423
  TotCalE= 78.5495
EventNo= 14
 BEAM= proton Mass= 938.272
  PXYZ= -194.629 -147.325 224.795 XYZi= 1236.62 1307.58 -1208.18
 NoCalHit= 6
  LogDID= 7 LogID= 6 LayerID= 0  DepE= 6.78486
  LogDID= 7 LogID= 7 LayerID= 0  DepE= 12.6713
  LogDID= 7 LogID= 17 LayerID= 1  DepE= 2.69791
  LogDID= 8 LogID= 17 LayerID= 1  DepE= 17.9847
  LogDID= 9 LogID= 17 LayerID= 1  DepE= 1.52024
  LogDID= 7 LogID= 29 LayerID= 2  DepE= 10.5675
  TotCalE= 52.2265
  ....
```

Figure 3.8: A part of CalOut.dat.

3.3.4 TKR

A sample of "TrackerOut.dat", output of the TKR, is shown in Figure 3.9. Event number and incident cosmic-ray information are printed at the beginning of each event as other outputs. "NoTrackerHit=" is a total number of hits (interaction) in the TKR in a event. ID number of hit silicon layer is represented in "SiID=". "ParSpc=" is a type of interacting particle. "TrkLen=", "XYZi=" and "XYZo=" are length of the step, the start point and end point of the step, respectively. Deposit energy is given in "DepE=". The total energy of the incident particle (before interaction) is also shown in "ParE=".

```
EventNo= 1
 BEAM= proton Mass= 938.272
  PXYZ= -7013.11 -16700.4 -3379.47 XYZi= 526.583 1803.74 908.729
 NoTrackerHit= 0
EventNo= 14
 BEAM= proton Mass= 938.272
  PXYZ= -194.629 -147.325 224.795 XYZi= 1236.62 1307.58 -1208.18
 NoTrackerHit= 7
  ID= 13  ParSpc= proton  TrkLen= 13.5797  XYZi= -123.218  -110.091  195.712
   XYZo= -130.729  -98.7852  195.312   DepE= 4.57604  ParE= 9617.41
  ID= 13  ParSpc= e-  TrkLen= 0.311348  XYZi= -127.87  -103.088  195.464
   XYZo= -127.849  -102.868  195.487   DepE= 0.186311  ParE= 0.778227
  ID= 13  ParSpc= e-  TrkLen= 0.0547406  XYZi= -127.849  -102.868  195.487
   XYZo= -127.835  -102.863  195.515   DepE= 0.080916  ParE= 0.591915
  ID= 13  ParSpc= e-  TrkLen= 0.0918037  XYZi= -124.184  -108.637  195.661
   XYZo= -124.159  -108.6  195.686   DepE= 0.110281  ParE= 0.62128
  ID= 13  ParSpc= e-  TrkLen= 0.493822  XYZi= -121.24  -113.59  195.712
   XYZo= -121.598  -113.697  195.617   DepE= 0.249601  ParE= 1.04359
  ID= 13  ParSpc= e-  TrkLen= 0.325221  XYZi= -121.598  -113.697  195.617
   XYZo= -121.718  -113.834  195.702   DepE= 0.174714  ParE= 0.793987
  ID= 13  ParSpc= e-  TrkLen= 0.0890789  XYZi= -121.718  -113.834  195.702
   XYZo= -121.695  -113.869  195.674   DepE= 0.108273  ParE= 0.619272
EventNo= 56
 BEAM= proton Mass= 938.272
  PXYZ= -5290.83 7987.87 -311.082 XYZi= 977.078 -1770.95 260.268
 NoTrackerHit= 0
  ....
```

Figure 3.9: A part of TrackerOut.dat.

3.4 Digitization/Conversion process

In order to simulate the real instruments and data acquisition system, we need to apply a digitization to Geant4 outputs, e.g., apply the threshold level, convert coordinate in the TKR to strip number and so on. We thus digitize/convert four Geant4 outputs and combine them into 1 file, named "G4Sim.irf". We separated this process from the Geant4 simulator, so that we can modify the digitization process without running the simulation again. We gave description of this process here. Flow chart of the process is shown in Figure 3.10, taken from the document by the simulation team [5].

As for the TKR, DigitizedTkr.pl converts the coordinates of the particle hits into the strip number (0-1599) corresponding to the hit. This script also judges if the hit position corresponds to "ladder gap" or "SSD gap" or "charge-share area" (Satou, [6]) and prints out the message in the output file (DigitizedTkr.dat) if the hit falls in one of these three regions. Then, DistributeEnergyTkr.pl calculates the charge-sharing effect and splices deposit energy into each strip. SimulateTkr.pl sums up energy deposition within each strip and throws away the hits below the threshold level (29.0 keV). Finally TriggerFilterTkr.pl converts the energy deposition into charge (2.25×10^{-5} GeV/fC, $\sim$ 3.6 eV to generate one electron-hole pair) and outputs the hit information of events that meet the Level 1 trigger condition; hit of three consecutive pairs of x and y SSD layers.

For the CAL, DigitizeCal.pl calculates the amount of energy at each end of a calorimeter log and SimulateCal.pl sums up deposit energies in each log. For each ACD tile and XGT block, deposit energies are already summed up in AntiOut.dat (output of ACD) and TargetOut.dat (output of XGTs), and thus there are no digitization scripts for these two kinds of detectors.

Finally, Convert2Irf.pl reads the digitized output of four detector components (TriggeredTkr.dat, SimulatedCal.dat, AntiOut.dat, and TargetOut.dat), applies the threshold level for the CAL, the ACD and the XGT, converts detector ID (Geant4 ID) into IRF ID, and outputs IRF-formatted result as G4Sim.irf. A sample of G4Sim.irf is shown in Figure 3.11. Once the Geant4 outputs are converted into an IRF file, we can convert it into the ROOT format and analyze simulation data in the same way as we analyze the BFEM data. Please see the reference [5] for more detail of IRF format and ID definition.

3.5 Running Tests of the Balloon Flight simulator

Before running the simulator, we need to confirm that the Geant4 simulator and conversion scripts work correctly. Below we briefly describe how we have checked the Geant4 simulator (§3.5.1) and digitization/conversion scripts (§3.5.2).

3.5.1 Tests of the Geant4 BFEM Simulator

We checked out whether the material and ID numbering are implemented correctly or not with using Geant4 output. To check out materials in the TKR and the CAL, we shot 3 GeV μ- to them and examined the energy loss in them. The mean values of measured energy losses agree with the theoretical values well. Thus we regard materials are implemented correctly. To check out the ID numbering in the simulator, we shot particles to each detector and examined Geant4 output and confirmed ID numbers are implemented correctly. Please see for more detail the document distributed by the simulation team [7].

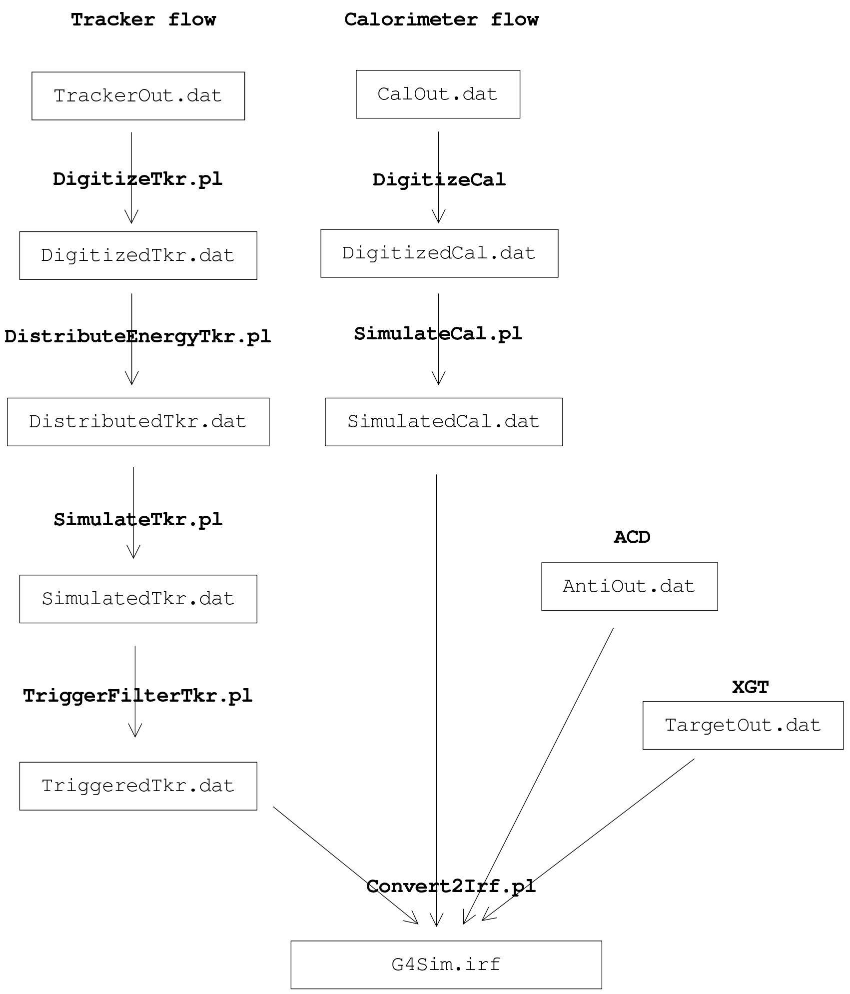

Figure 3.10: Flow chart of digitization/conversion process.

```
1 37 proton 32.796720 -172.033 52.348 80.934 869946 -182443 -458155 |
412 6.532 3 1146 6.532 0 1164 1.852 0 1165 3.959 0 |
413 6.942 3 259 6.168 0 260 3.637 0 273 6.942 0 |
414 6.451 3 126 6.451 0 243 5.125 0 261 5.031 0 |
415 12.352 4 1040 3.667 0 1041 9.267 0 1101 12.352 0 1125 5.059 0 |
416 5.475 2 958 4.537 0 1056 5.475 0 |
417 6.442 2 213 6.442 0 260 5.817 0 |
425 5.908 4 144 3.762 0 145 2.315 0 254 3.888 0 255 5.908 0 |
426 8.287 3 179 8.287 0 263 2.984 0 264 2.984 0 |
427 4.703 2 142 4.612 0 143 4.703 0 |
428 3.776 1 0 3.776 0 |
429 6.312 2 246 6.312 0 247 2.934 0 |
447 0.002145 |
445 0.006052 |
-1
1 141 proton 3.549241 47.989 -169.535 89.808 -189918 895499 -402503 |
409 11.377 2 1237 11.377 0 1238 7.419 0 |
410 14.753 1 1297 14.753 0 |
411 4.653 5 1213 4.630 0 1214 4.653 0 1215 4.653 0 1216 4.653 0 1217
2.177 0 |
412 4.501 5 894 4.501 0 895 4.501 0 896 4.501 0 897 4.501 0 898 2.317 0
|
413 14.998 1 1384 14.998 0 |
414 12.636 1 1455 12.636 0 |
415 2.503 4 501 2.503 0 502 2.503 0 503 2.503 0 504 2.503 0 |
417 14.560 2 1540 2.842 0 1541 14.560 0 |
446 0.002035 |
-1
  ....
```

Figure 3.11: A part of IRF-formatted G4Sim.irf. Information of each event is listed between lines with 1 to -1 in first column. ID numbers of detectors are also shown in the same column. Please see the reference [5] for more detail of IRF format.

3.5.2 Digitization/Conversion Scripts

To check out whether our simulator and digitization process work correctly or not, we shot 1 million cosmic-ray protons to the whole pressure vessel and ran the digitization/conversion script to the obtained outputs with default threshold level for all detectors, and examined results, G4Sim.irf. This is summarized in the document prepared by the simulation team [8]. Below we briefly describe what we have checked.

XGT

We made the deposit energy distribution of XGTs from G4Sim.irf as shown in Figure 3.12. Geant4 IDs are converted in IRF IDs; ID 0, 1, 2 and 3 in Geant4 corresponds to ID 450, 451, 452 and 453 in IRF, respectively. Here, the threshold level is tentatively set at 400 keV in the scripts and applied correctly. Although the statistics are somewhat poor, we can see a hump around 10 MeV, corresponding to the energy deposition of MIP proton that passed the XGT. This fact shows that our simulator appropriately handle the element compositions and density of the XGT scintillator.

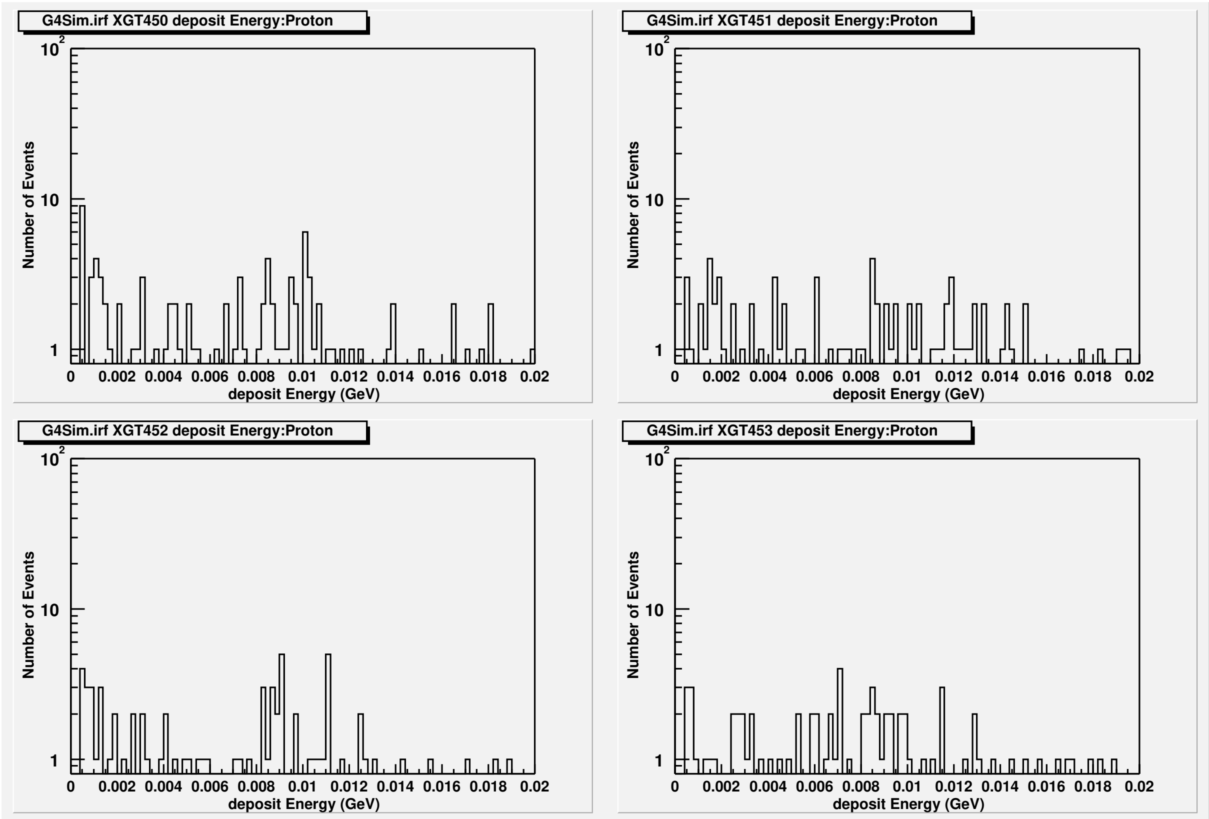

Figure 3.12: Distribution of deposit energy in XGTs, derived from G4Sim.irf. Energy threshold level is set at 400 keV.

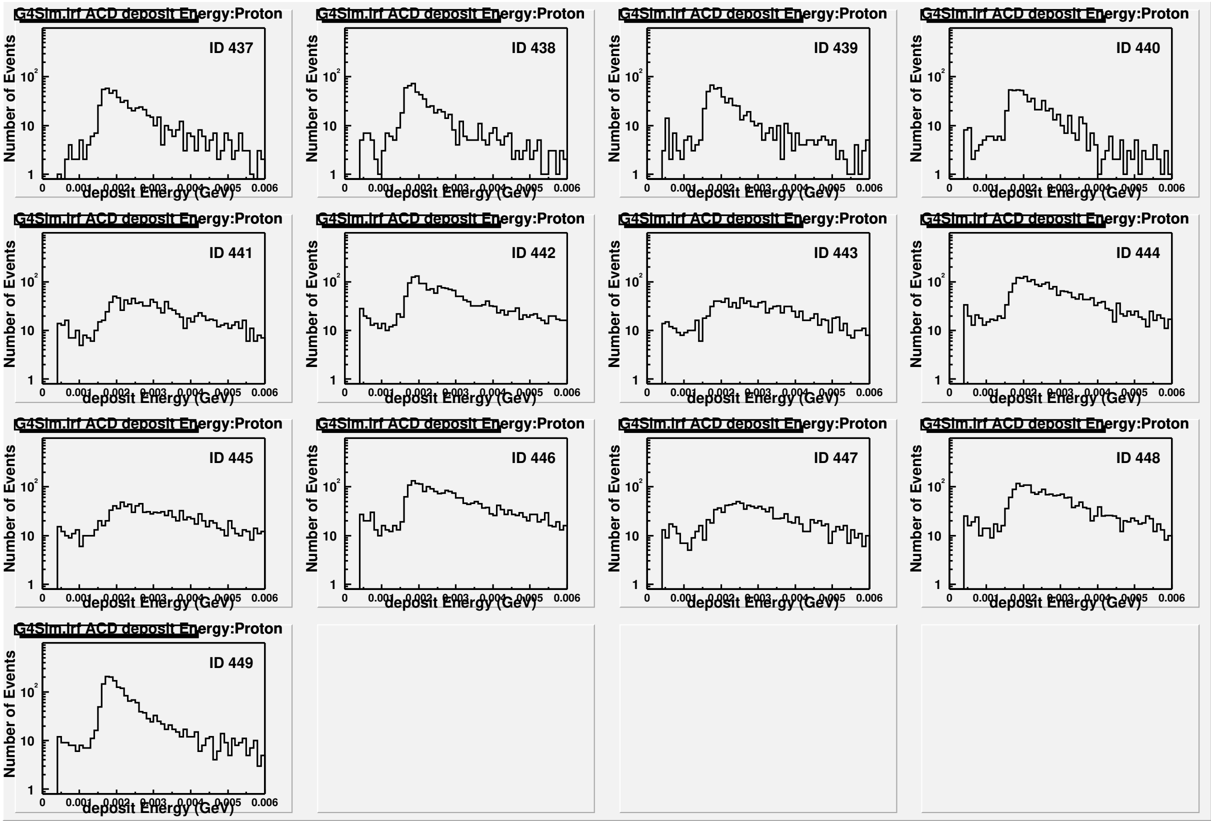

Figure 3.13: Distribution of deposit energy in ACDs, derived from G4Sim.irf. Energy threshold level is set at 400 keV.

ACD

ID numbers are converted from Geant4 IDs to IRF IDs in G4Sim.irf. The relation of two ID numbering are given in Table 3.10. Similar to XGT, we made plots of energy deposition from G4Sim.irf as shown in figure 3.13. The default threshold value for ACD is 400 keV and applied correctly. We can also see the peak around 2 MeV, corresponding to MIP peak in ACD. We thus conclude that our simulator/digitizer appropriately handle the ACD.

Table 3.10: The relation between Geant4 IDs and IRF IDs for ACD.

Geant4 ID	20	21	15	14	8	2	9	3	10	4	7	19	13
IRF ID	437	438	439	440	441	442	443	444	445	446	447	448	449

CAL

We made plots of energy distribution for all CsI logs from G4Sim.irf. Geant4 IDs are converted to IRF IDs as follows,

$$\text{IRFID} = 2 + 5 \times (10 \times (7 - \text{LayerID}) + (\text{LogID})),$$

Figure 3.14: Distribution of deposit energy in CAL, derived from G4Sim.irf. Energy threshold level is set at 0 keV.

when logs are oriented along y axis, and

$$\text{IRF ID} = 2 + 5 \times (10 \times (7 - \text{LayerID}) + (9 - \text{LogID})),$$

when logs are oriented along x axis. The default threshold value is 0 keV for CAL. The obtained results are summarized in Figure 3.14, implying that all the CsI logs are active in our simulator and digitization/conversion scripts. We can see humps around 15 MeV corresponds to the MIP peak of proton.

TKR

In G4Sim.irf, Geant4 IDs are converted to IRF IDs as follows

$$\text{IRFID} = 404 + \text{LayerID},$$

where 404 is the bottommost tray and 429 is the topmost tray. Layers from 420 to 429 are incomplete layers (not all SSDs are placed in a layer). We made the histogram of number of hits in each strip from G4Sim.irf as shown in Figure 3.15. Hit strips distribute widely (0-1599 strips) in each layer because protons are shot to the whole pressure vessel. The figures show that our BFEM simulator implements the incomplete layers appropriately.

We last made the distribution of the number of hit layers, shown in Figure 3.16, to check out whether trigger condition is applied correctly or not. The events in which the

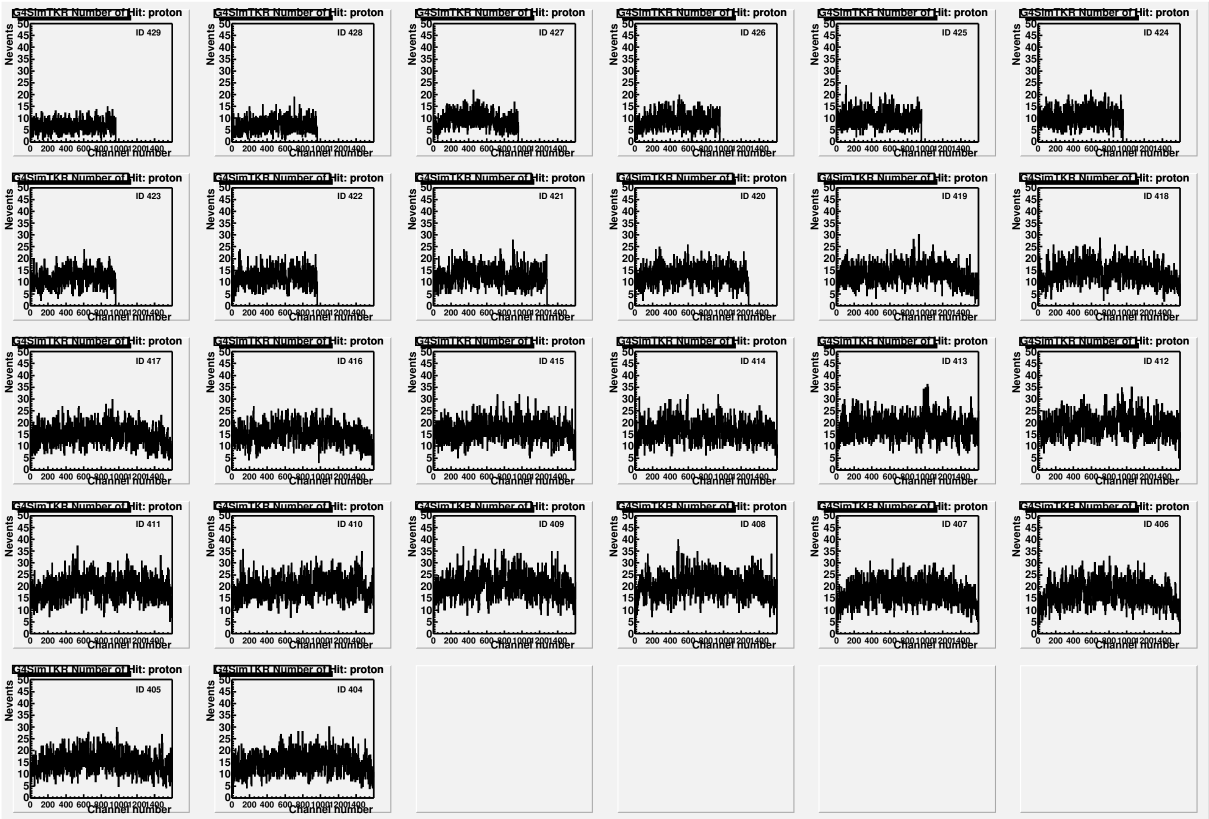

Figure 3.15: Distribution of the number of hits in each strip, derived from G4Sim.irf.

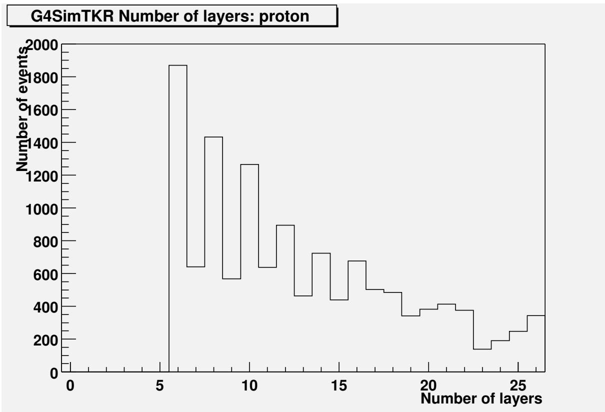

Figure 3.16: Distribution of number of hit layers, derived from G4Sim.irf. The minimum number of hit layers is 6, following the Level 1 Trigger condition.

number of hit layers was less than five were thrown away. Thus, we conclude scripts treat the Level 1 trigger correctly.

Chapter 4

Cosmic-Ray Generator for the GLAST Balloon Flight

We have developed cosmic-ray generators as well as a BFEM geometry model (see Chapter 3), and this work was mainly done by M.Ozaki, K.Hirano, Y.Fukazawa and T.Mizuno. The cosmic-ray background models are based on the measurements and both a primary and a secondary component are constructed. Spectrum of cosmic-rays highly depends on a local geomagnetic coordinate and solar activity. These effects are described by two parameters, geomagnetic cutoff rigidity and solar modulation potential. The model parameters of geomagnetic cutoff and solar modulation effects are fixed at those of Palestine in 2001 in our analysis. An application of models to entire low earth orbit of an arbitary solar cycle is straightforward. In this chapter we describe those cosmic-ray background models.

4.1 Effect of Solar Activity and Geomagnetic field on Primary Particles

Cosmic-rays, highly accelerated particles, propagate through the universe and enter the earth. They are called primary cosmic-rays and the main component is known to be protons. When primary particles penetrate into the air, they interact with molecules of the air and produce relatively low-energy particles, called secondary cosmic-rays. We need to implement both “primary” and “secondary” component in the simulator.

Since primary particles come from outside the solar system, their spectra are affected by the solar activity and earth geomagnetic field. Primary cosmic-rays are bent by geomagnetic field around the earth hence low-energy particles cannot reach to the earth. We implemented those “geomagnetic cutoff effect” and “solar modulation” for the primary component in our models, and represent the spectra as described below.

4.1.1 Solar modulation

Cosmic-rays entering the solar system are decelerated by the solar wind, an expanding magnetized plasma flow ejected from the sun. Thus, primary cosmic-ray spectra measured on the earth highly depends on solar activity, and the flux of primary particles anti correlates with solar activity. The effect of this “solar modulation” has been studied and is represented by an effective energy shift of the spectrum as below

$$Mod(E) = Unmod\,(E + e\Phi) \times \frac{E^2 - {E_0}^2}{(E + e\Phi)^2 - {E_0}^2}[9]. \tag{4.1}$$

where E and E_0 represent the total and rest energy of the particle, respectively, e is the electron charge and Φ gives solar modulation parameter (called solar potential), and $Mod\ (E)$ and $Unmod\ (E)$ are the spectra after and before suffering modulation. For the GLAST balloon experiment, we adapt $\Phi = 1100$ MV, typical value for solar maximum activity.

4.1.2 Geomagnetic cutoff

When cosmic-rays approach the earth, a trajectory of particles is affected by the geomagnetic field, and low-energy particles go away outside the earth. The Ramour radius ρ of a charged particle in magnetic field is expressed as

$$\rho = \frac{pc}{q} \times \frac{1}{cB} = \frac{R}{cB} \tag{4.2}$$

where c denotes the light speed, p and q are the momentum and charge of the particle, and B is the magnetic field. Here, $R \equiv \frac{pc}{q}$ is called rigidity and has a dimension of a voltage. Substituting typical values in eq. 4.2, e.g., $\rho = 650$ km ($\frac{1}{10}$ earth radius) and $B = 0.4$ gauss, R becomes ~ 8 GV. Thus, cosmic-rays with rigidity below 10 GV are strongly affected by the geomagnetic field. It is convenient to define a value called cutoff rigidity; particles with rigidity below this value cannot penetrate the earth. Assuming the earth magnetic field to be the dipole shape, this value ($R_{\rm cutoff}$) is calculated as

$$R_{\rm cutoff}(\mathrm{GV}) = 14.9 \times \left(1 + \frac{h}{R_{\rm earth}}\right)^{-2} \times (\cos\theta_{\rm M})^4\,, \tag{4.3}$$

where h is the altitude and $R_{\rm earth}$ is the earth radius. $\theta_{\rm M}$, called geomagnetic latitude, is a latitude in geomagnetic coordinate system ($\theta_M = 0$ radian at geomagnetic equator and $\frac{\pi}{2}$ radian at the geomagnetic north pole) [10], [11]. For the Balloon experiment, substituting $h \sim 35$ km, $\theta_{\rm M} = 42.15°$ (0.735 radian) and $R_{\rm earth} = 6380$ km, we obtain

$$R_{\rm cutoff}(\mathrm{GV}) = 4.46\ \mathrm{GV}.$$

To express the geomagnetic cutoff effect, we refer to the AMS data [12] and represent the attenuation factor as follows,

$$\mathrm{CutOff}(R) = \frac{1}{1 + \left(\frac{R}{R_{\rm cutoff}}\right)^{-12.0}},$$

where R is the rigidity of the particle.

4.2 Proton Model

4.2.1 Primary Component

Proton is known to be a main component of cosmic-rays. As for the primary proton spectrum, we refer to two experimental data; AMS [12] and BESS [13]. The BESS experiment provides us with the most accurate data near the geomagnetic north pole. The AMS experiments have measured the flux at many different geomagnetic latitudes and provides us with the most accurate spectra around the geomagnetic cutoff. The spectrum near the polar region for both experiments agree with each other within 15 %. Hereafter we refer to the AMS data, and expresses the spectrum before solar modulation as,

$$Unmod\,(E) = 16.9 \times \left(\frac{pc}{\mathrm{GeV}}\right)^{-2.79} \quad [\mathrm{MeV}^{-1}\mathrm{m}^{-2}\mathrm{s}^{-1}\mathrm{sr}^{-1}].$$

After entering the solar system, particles suffer the influence of the solar wind and the flux is modulated as eq. 4.1, where $\Phi = 1100$ MV (solar maximum) and E_0 is the mass of proton, 0.938 GeV. Next we included the geomagnetic cutoff effect as

$$J_{\mathrm{primary}(E)} = Mod(E) \times \frac{1}{1 + (R/R_{\mathrm{cutoff}})^{-12.0}} \times \beta, \tag{4.4}$$

where R_{cutoff} is the cutoff rigidity at Palestine, Texas ($R_{\mathrm{cutoff}} = 4.46$ GV). The spectrum is measured as the number of particles that passed the detector per unit time. To represent this fact, we introduced $\beta = v/c$. The angular distribution is assumed to be uniform and independent of the incident angle for zenith angle of $\theta \leq 90°$, where $\theta = 0°$ means the particle going vertically downward. For $\theta \geq 90°$, particles are blocked by the earth and the flux becomes zero.

4.2.2 Secondary Component

Secondary cosmic-rays are produced by the interaction of primary cosmic rays with molecules in the atmosphere. They are divided into two parts, "splash" and "re-entrant". "Splash" is upward moving particles generated in the atmosphere, and "re-entrant" is downward moving particles and observed as particles whose rigidities are below the local geomagnetic rigidity. The flux of secondary cosmic-rays is measured in several rocket- or balloon-borne experiments and in the AMS experiment. The spectra of splash and re-entrant are almost the same near geomagnetic equator but the flux of re-entrant becomes larger than that of splash as we approach the geomagentic pole. The difference of spectra between re-entrant and splash are small at Palestine ($\theta_M = 0.735$ radian). Thus we implemented spectra of them with the same shape for simplicity. There is no available data on spectra below 100 MeV. Thus we extrapolated the power-law spectrum of index = -1 based on thoretical prediction in this energy range. The vertical upward or downward spectrum is represented as

$$J_{\mathrm{splash}}(E_{\mathrm{k}}) = J_{\mathrm{re-entrant}}(E_{\mathrm{k}}) = 3 \times 10^{-3} \times \left(\frac{E_{\mathrm{k}}}{\mathrm{GeV}}\right)^{-2.5} \times e^{(-E_{\mathrm{k}}/E_{\mathrm{cutoff}})^{-1}} [\mathrm{MeV}^{-1}\mathrm{m}^{2}\mathrm{s}^{-1}\mathrm{sr}^{-1}],$$

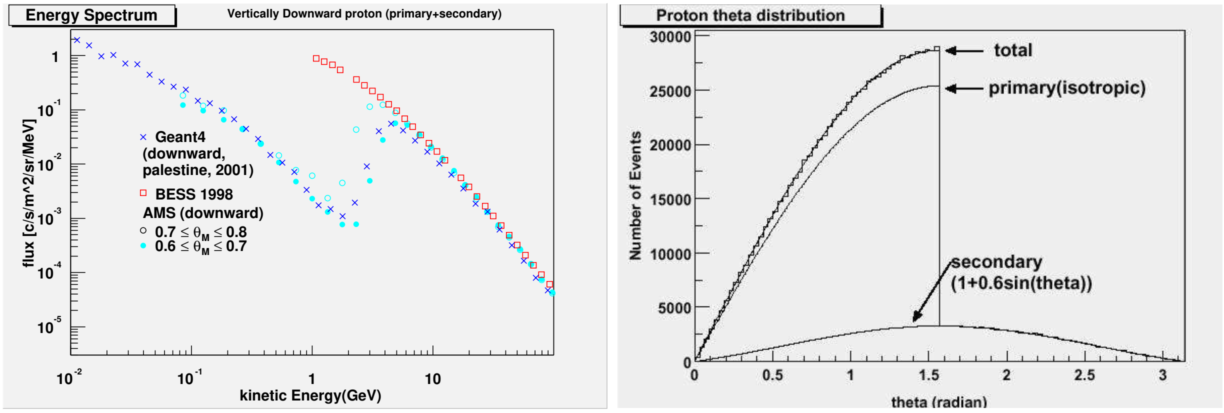

Figure 4.1: Left) Energy spectrum of proton. Geant4-generated proton spectrum is shown with AMS data and BESS data. Right) Zenith angle dependence of the flux in our program.

in 100 MeV $\leq E_k \leq$ 10 GeV, where E_k is the kinetic energy of a particle and $E_{cutoff} =$ 0.16 GeV. Below 100 MeV, the spectra are expressed as

$$J_{splash}(E_k) = J_{re-entrant}(E_k) = 1.92 \times 10^{-2} \times \left(\frac{E_k}{\mathrm{GeV}}\right)^{-1} [\mathrm{MeV}^{-1}\mathrm{m}^2\mathrm{s}^{-1}\mathrm{sr}^{-1}].$$

The zenith angle dependence of flux was not measured in the AMS experiment but an increase of the flux near horizontal direction was detected in several old experiments [14], [15], where the dependence is represented as

$$J(E_k, \theta) = (1 + 0.6 \sin\theta) \times J_{\text{splash or re-entrant}}(E_{k,\theta=0}).$$

and we adopted this dependence for our generator. The spectrum of our model and zenith angle dependence are shown in Figure 4.1.

4.3 Electron Model

4.3.1 Primary Component

No single experiment has yet measured the primary electron energy spectrum in a wide energy range. We thus used the data compilation of measurements of Komori et al, and took the power-law fit given there (Figure 4.2). The energy of primary electrons shown in Figure 4.2 is sufficiently high that we can regard the spectrum do not suffer the solar activity. Therefore,

$$Unmod(E) = 0.723 \times \left(\frac{pc}{\mathrm{GeV}}\right)^{-3.33} [\mathrm{MeV}^{-1}\mathrm{m}^{-2}\mathrm{s}^{-1}\mathrm{sr}^{-1}].$$

Modulations by solar activity and geomagnetic cutoff effect are represented in the same way as for protons. The angular distribution is thought to be uniform and independent on the angle.

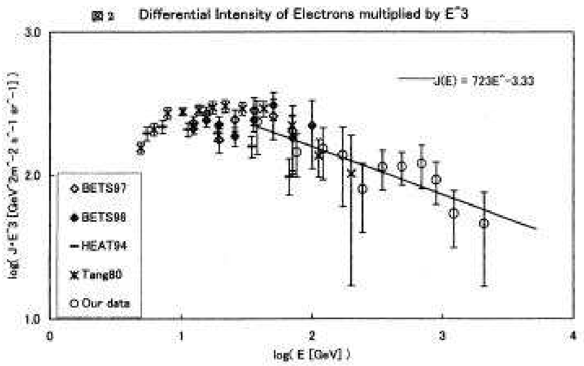

Figure 4.2: Energy spectrum of the primary electron taken from Y.Komori et al [16].

4.3.2 Secondary Component

Secondary electrons are mainly produced by muon decay. The AMS experiment measured the spectra of downward and upward electron in 0.2 to 40 GeV range at many different geomagnetic latitudes as shown in Figure 4.3. Upward component has a spectral shape similar to that of the proton. For the downward component, on the other hand, the valley between the cutoff primary spectrum and the power-law secondary spectrum is filled by a new component at high geomagnetic latitudes (Figure4.3). We modeled this third component as a hump in the spectrum. Our model for splash electron is represented by

$$J_{\mathrm{splash}} = 1.33 \times 10^{-4} \times \left(\frac{E_{\mathrm{k}}}{\mathrm{GeV}}\right)^{-3.53} \quad [\mathrm{MeV}^{-1}\mathrm{m}^{-2}\mathrm{s}^{-1}\mathrm{sr}^{-1}]$$

in 100 MeV $\leq E_{\mathrm{k}} \leq$ 10 GeV, and model for re-entrant is expressed as

$$J_{\mathrm{re-entrant}} = 1.33 \times 10^{-4} \times \left(\frac{E_{\mathrm{k}}}{\mathrm{GeV}}\right)^{-3.53} [\mathrm{MeV}^{-1}\mathrm{m}^{-2}\mathrm{s}^{-1}\mathrm{sr}^{-1}]$$

when 0.1 GeV $\leq E_{\mathrm{k}} \leq$ 0.6 GeV or 6 GeV $\leq E_{\mathrm{k}} \leq$ 10.0 GeV. Between 0.6 GeV and 6 GeV, the spectrum is expressed as

$$J_{\mathrm{re-entrant}} = 1.33\times10^{-4}\times\left(\frac{E_{\mathrm{k}}}{\mathrm{GeV}}\right)^{-3.53} + 2.0\times10^{-4}\times\left(\frac{E_{\mathrm{k}}}{\mathrm{GeV}}\right)^{2}\times e^{-\left(\frac{E_{\mathrm{k}}}{E_{\mathrm{cutoff}}}\right)^{3}} [\mathrm{MeV}^{-1}\mathrm{m}^{-2}\mathrm{s}^{-1}\mathrm{sr}^{-1}]$$

where E_{cutoff} = 3.2 GeV. In 10 MeV $\leq E_{\mathrm{k}} \leq$ 100 MeV, there is no reliable data and we modeled spectrum as power-law with index of -1,

$$J_{\mathrm{splash}} = J_{\mathrm{re-entrant}} = 4.51 \times 10^{-2} \times \left(\frac{E_{\mathrm{k}}}{\mathrm{GeV}}\right)^{-1.0} [\mathrm{MeV}^{-1}\mathrm{m}^{-2}\mathrm{s}^{-1}\mathrm{sr}^{-1}].$$

We implemented zenith angle dependence for both splash and re-entrant components as $(1 + 0.6 \sin\theta)$. The flux of AMS data and our model are shown in Figure 4.4 and zenith angle dependence is in Figure 4.5.

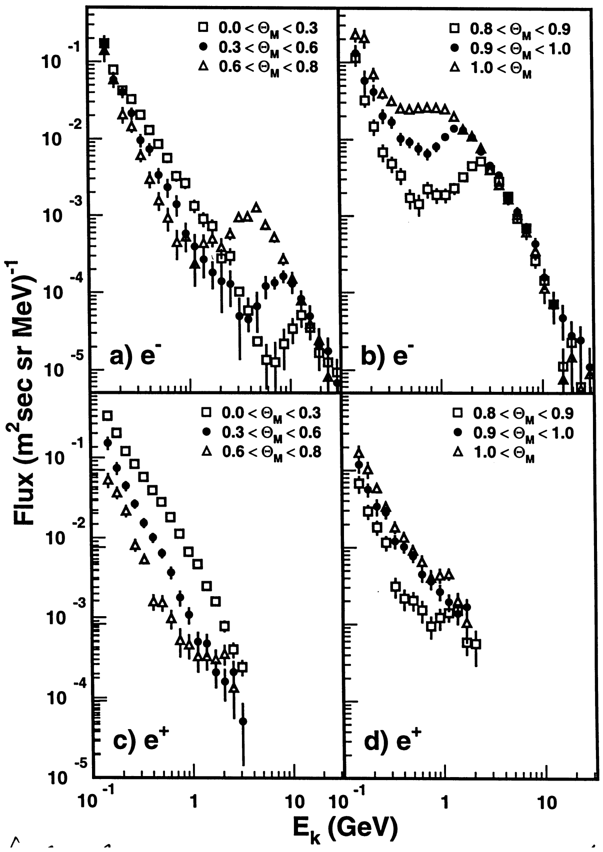

Figure 4.3: Energy spectra of electron and positron measured in AMS experiment. As for downward component, the valley between the geomagnetic cutoff of the primary and the power-law secondary is filled by a third component.

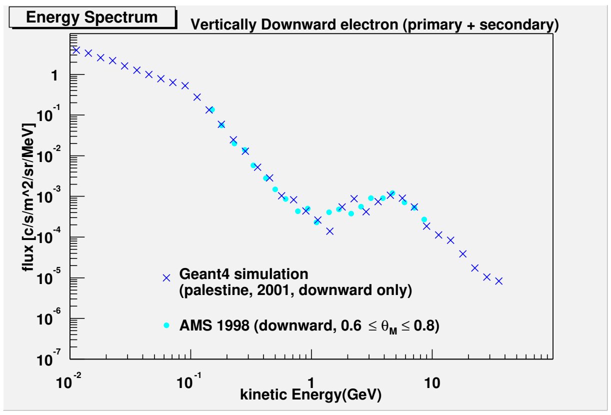

Figure 4.4: Electron energy spectrum of our model, together with AMS data.

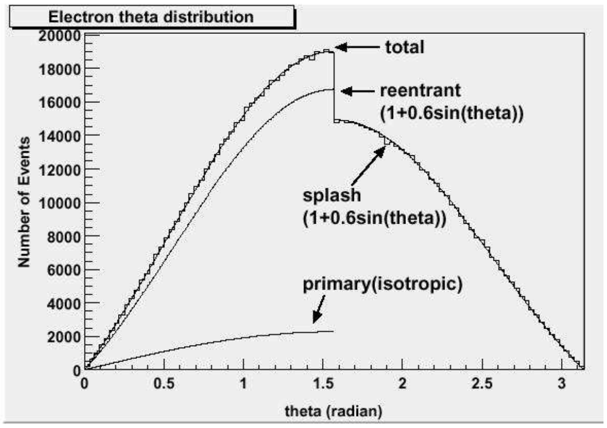

Figure 4.5: Zenith angle dependence of our electron model.

4.4 Spectral models of other particles

4.4.1 Positron Model

A fraction of primary positrons and electrons, defined as $\frac{e^+}{e^+ + e^-}$, has been measured by several experiments. Among them, Golden et al [18] measured the fraction in high energy range ($\sim$ 5 to 60 GeV) and showed that it is consistent with a constant fraction of 0.078 $\pm$ 0.016. We adopted their results and modeled the primary positron spectrum as

$$Unmod\,(E) = 0.0564 \times \left(\frac{pc}{\mathrm{GeV}}\right)^{-3.33} \quad [\mathrm{MeV^{-1}m^{-2}s^{-1}sr^{-1}}].$$

Modulations by solar activity and geomagnetic cutoff effect are taken into account in the same way as for electrons. The flux distributes uniformly on zenith angle ($0 \leq \theta \leq \pi/2$) and azimuth angle ($0 \leq \theta \leq 2\pi$). For secondary component, we refered to the AMS experiment [17] above 0.1 GeV (Figure 4.3). Then the re-entrant (vertically downward going) spectrum is expressed as

$$J_{\mathrm{re-entrant}} = 2.12\times10^{-4}\times\left(\frac{E_{\mathrm{k}}}{\mathrm{GeV}}\right)^{-3.09} + 3.0\times10^{-4}\times\left(\frac{E_{\mathrm{k}}}{\mathrm{GeV}}\right)\times e^{-\left(\frac{E_{\mathrm{k}}}{E_{\mathrm{cutoff}}}\right)^2} [\mathrm{MeV^{-1}m^{-2}s^{-1}sr^{-1}}]$$

where $E_{\mathrm{cutoff}} = 2.0$ GeV, and the splash (vertically upward going) spectrum becomes

$$J_{\mathrm{splash}} = 2.12 \times 10^{-4} \times \left(\frac{E_{\mathrm{k}}}{\mathrm{GeV}}\right)^{-3.09} \quad [\mathrm{MeV^{-1}m^{-2}s^{-1}sr^{-1}}].$$

As in the case of electron, there is no reliable data for positron spectrum below 100 MeV. Therefore, we just extrapolated the spectrum below 100 MeV as

$$J_{\mathrm{re-entrant}} = J_{\mathrm{splash}} = 2.61 \times 10^{-2} \times \left(\frac{E_{\mathrm{k}}}{\mathrm{GeV}}\right)^{-1} \quad [\mathrm{MeV^{-1}m^{-2}s^{-1}sr^{-1}}].$$

We assumed the same angular dependence as that of proton and electron secondaries. The data by AMS and spectrum generated by our model are shown in Figure 4.6.

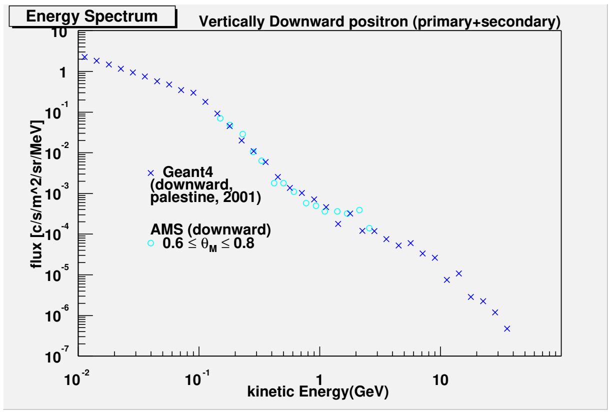

Figure 4.6: Geant4-generated positron spectrum with AMS data.

4.4.2 $\mu^{\pm}$ Model

Since the life time of $\mu^{\pm}$ is short, we can neglect primary component. The spectrum of secondary $\mu^{\pm}$ is reported by M.Boezio et al [19]. They measured downward $\mu^{\pm}$ in 0.2-10 GeV band. Refering to their data, we modeled vertically upward and downward μ^{-} spectra as

$$J_{\mathrm{re-entrant}} = J_{\mathrm{splash}} = 6.5 \times 10^{-3} \times \left(\frac{E_{\mathrm{k}}}{\mathrm{GeV}}\right)^{-2.21} \quad [\mathrm{MeV}^{-1}\mathrm{m}^{-2}\mathrm{s}^{-1}\mathrm{sr}^{-1}]$$

above 1 GeV and

$$J_{\mathrm{re-entrant}} = J_{\mathrm{splash}} = 6.5 \times 10^{-3} \times \left(\frac{E_{\mathrm{k}}}{\mathrm{GeV}}\right)^{-1} \quad [\mathrm{MeV}^{-1}\mathrm{m}^{-2}\mathrm{s}^{-1}\mathrm{sr}^{-1}]$$

below 1 GeV. The reference data were obtained at the polar region, whereas our Balloon Experiment was performed at $R_{\mathrm{cutoff}} \sim 4.5$ GV. Therefore, the true spectral shape and normalization are somewhat uncertain.

The ratio of μ^{+} to μ^{-}, $\frac{\mu^{+}}{\mu^{-}}$, is found to be 1.6 in [19], thus we modeled the μ^{+} spectrum with same spectral shape but 1.6 times higher normalization. There is no available data about angular dependence of the flux. We assumed that the flux of $\mu^{\pm}$ have the same zenith angle dependence as that of $\mathrm{e}^{\pm}$, because $\mu^{\pm}$ decay into $\mathrm{e}^{\pm}$ and they might have similar angular distribution with that of $\mathrm{e}^{\pm}$. Comparison between the Geant4 generated spectra and those of Boezio et al are shown in Figure 4.7.

4.4.3 Gamma-ray Model

We first modeled extra galactic diffuse gamma-rays obtained by several gamma-ray satellites [20] as primary component. The spectrum is expressed as three power-law functions. In 30-50 keV it is expressed as

$$J_{\mathrm{primary}} = 570.8 \times \left(\frac{E}{\mathrm{MeV}}\right)^{-1.86} \quad [\mathrm{MeV}^{-1}\mathrm{m}^{-2}\mathrm{s}^{-1}\mathrm{sr}^{-1}],$$

and in 50 keV-1 MeV

$$J_{\mathrm{primary}} = 40.0 \times \left(\frac{E}{\mathrm{MeV}}\right)^{-2.75} \quad [\mathrm{MeV}^{-1}\mathrm{m}^{-2}\mathrm{s}^{-1}\mathrm{sr}^{-1}],$$

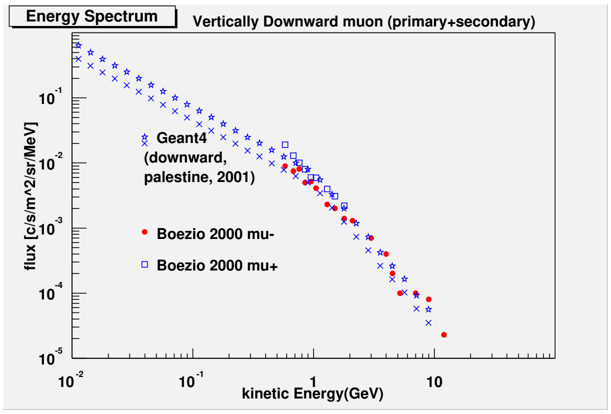

Figure 4.7: Geant4-generated $\mu^{\pm}$ spectrum with data by Boezio et al.

and in 1 MeV-100 GeV

$$J_{\rm primary} = 40.0 \times \left(\frac{E}{\rm MeV}\right)^{-2.15} \quad [{\rm MeV^{-1}m^{-2}s^{-1}sr^{-1}}].$$

The flux is independent of zenith angle in $(0 \leq \theta \leq \pi/2)$.

Secondary gamma-rays are mainly generated by bremsstrahlung of $e^{\pm}$ produced in the atmosphere. The spectrum of vertically downward-going gamma-rays at Palestine is compiled in [21] and [22]. We scaled these data to the residual atmosphere of 3.8 g/cm^2 (our experiment) and modeled spectrum as follows. In 1-1000 MeV the spectrum becomes

$$J_{\rm downward} = 250.0 \times \left(\frac{E}{\rm MeV}\right)^{-1.70} + 1.14 \times 10^5 \times \left(\frac{E}{\rm MeV}\right)^{-2.5} \times e^{-\left(\frac{E}{E_{\rm cutoff}}\right)^{-1.5}} \quad [{\rm MeV^{-1}m^{-2}s^{-1}sr^{-1}}],$$

where $E_{\rm cutoff} = 120$ MeV, and in 1-100 GeV

$$J_{\rm downward} = 2.15 \times 10^4 \times \left(\frac{E}{\rm MeV}\right)^{-2.20} \quad [{\rm MeV^{-1}m^{-2}s^{-1}sr^{-1}}].$$

Since we could not find reliable observational data below 1 MeV, we assumed the same spectral shape as upward component (see below) and expressed the spectrum as

$$J_{\rm downward} = 250.0 \times \left(\frac{E}{\rm MeV}\right)^{-1.34} \quad [{\rm MeV^{-1}m^{-2}s^{-1}sr^{-1}}].$$

in 30 keV-1 MeV. We also included 511 keV annihilation line of 70.5 [cm^{-2}s^{-1}sr^{-1}] based on [23]. Vertically downward spectrum generated by our program is shown in Figure 4.8 with reference data. As for vertically upward component, we refered to [23] - [26] and modeled as follows. In 30keV-1 MeV the spectrum is

$$J_{\rm upward} = 1670 \times \left(\frac{E}{\rm MeV}\right)^{-1.34} \quad [{\rm MeV^{-1}m^{-2}s^{-1}sr^{-1}}].$$

In 1-1000 MeV

$$J_{\rm upward} = 1670 \times \left(\frac{E}{\rm MeV}\right)^{-1.70} \quad [{\rm MeV^{-1}m^{-2}s^{-1}sr^{-1}}].$$

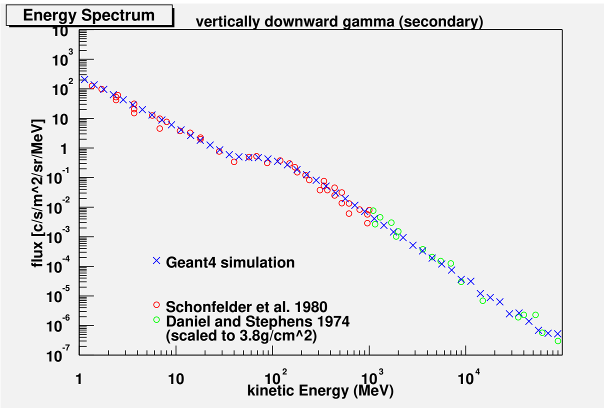

Figure 4.8: Geant4-generated vertically downward atmospheric gamma spectrum with experimental data by V.Schönfelder and by Daniel and Stephens.

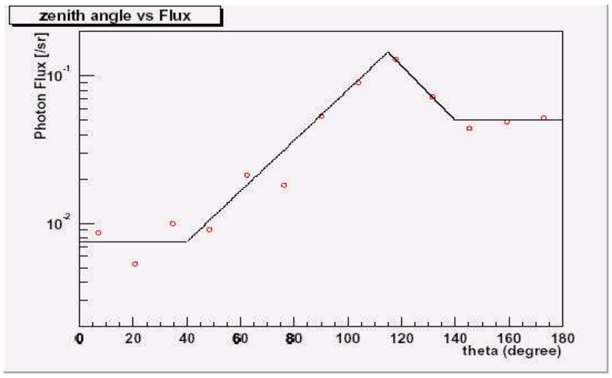

Figure 4.9: Zenith angle dependence of secondary gamma-ray. Red circles are observed data measured by V.Schönfelder, et al (after applying correction of atmospheric depth; see text) and solid line is our model function.

In 1-100 GeV

$$J_{\mathrm{upward}} = 5.29 \times 10^4 \times \left(\frac{E}{\mathrm{MeV}}\right)^{-2.20} \quad [\mathrm{MeV}^{-1}\mathrm{m}^{-2}\mathrm{s}^{-1}\mathrm{sr}^{-1}].$$

We also added 511 keV line emission with the intensity of 470 [$\mathrm{cm}^{-2}\mathrm{s}^{-1}\mathrm{sr}^{-1}$] based on [23]. Angular dependence of the secondary gamma-ray flux has been measured by several authors ([26], [27]) and known to depend strongly on zenith angle. We constructed the model function refering to [27], where they measured the gamma-ray flux in 1.5-10 MeV region at 2.5 g/cm^2. We multiplied their data between $0^\circ \leq \theta \leq 90^\circ$ (i.e., downward component) by 3.8/2.5 to correct the atmospheric depth and expressed the angular dependence as shown in Figure 4.9. We assumed the spectrum shape of both downward component ($0 \leq \theta \leq \pi/2$) and upward one ($\pi/2 \leq \theta \leq \pi$) does not depend on the zenith angle.

Chapter 5

Comparison between the Simulation and the Balloon Flight Data

In this chapter, we have ran the balloon flight simulator composed of a geometry model and cosmic-ray background models, and compared the balloon experiment data and the simulation results. Based on comparative results, we have tuned both the geometry and cosmic-ray models in the simulator up to develop reliable detector simulator and cosmic-ray models and to analyze cosmic-ray environment. The comparison is required to be done based on several informations, i.e., informations of the TKR, CAL, ACD and XGT. As a first step of the analysis, we compared the trigger rate and the TKR hit information, i.e., a count rate of each SSDs layer and the number of hit SSDs layer in an event. These information enable us to compare the detector response to the cosmic-ray environment directly. We classified events in two kinds, i.e., charged events and neutral events, to make comparison systematically. Charged events are such events in which one or more ACD tiles have energy deposit above a threshold level of 0.38 MeV $\approx$ 0.2 MIP. Neutral events correspond to events in which ACD tiles do not have a hit, and gamma-ray events are dominant as described below.

5.1 Energy Range of Cosmic-Ray Models

Before discussing the simulation data, we first examine whether the energy range of each cosmic-ray model (Chapter 4) is sufficiently wide or not.

An energy range of the cosmic-ray proton model is 10 MeV - 100 GeV, and energy spectrum of triggered cosmic-ray proton is shown in Figure 5.1. Blue, Red and green line represent all events, charged events and neutral events, respectively. More than 97 % is classified into charged events. As for both charged and neutral events, a trigger efficiency drops quickly below 100 MeV. We estimate the number of triggered events above 100 GeV protons by assuming the same slope as that of 10-100 GeV. The number of events in 100-1000 GeV range will be below $\sim$4 % of that in 10 MeV to 100 GeV energy range. Thus a energy range of the proton model is sufficiently wide to discuss the trigger rate. Energy spectrum of triggered electron is shown in Figure 5.2. We can see the trigger efficiency is dropping below 100 MeV. We estimated the number of events from 100 to 1000 GeV the same way as that of proton and found that it is a few percent of all events. We also estimated the number of events below 10 MeV by assuming the same slope of

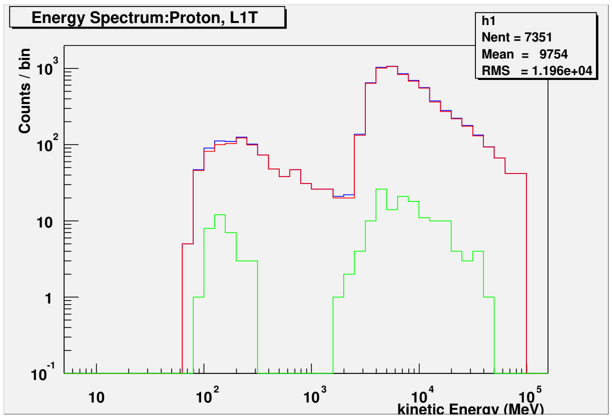

Figure 5.1: Energy spectrum of triggered cosmic-ray proton. That of all, charged and neutral events are shown in blue, red and green line, respectively.

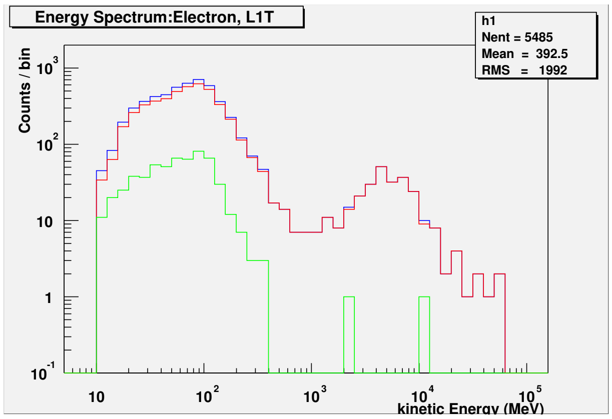

Figure 5.2: Energy spectrum of triggered cosmic-ray electron.

10 to 100 MeV. The number of events in the region turned out to be below 1 % for all events. ¡Thus a energy range of the electron model is wide enough. We also confirmed that the energy range of the other particle is sufficiently wide.

5.2 Comparison between the Balloon Data and the Simulation

The balloon flight data is divided into two parts, i.e., data during the ascent and that of the level flight (Figure 2.4). In this thesis, we have compared the level flight data and the simulation since the radiation environment was stable and similar to that of low-earth orbit. The balloon data during the level flight was mainly analyzed by T.Mizuno [28], and the trigger rate was found to be constant of $\sim$ 500 Hz (Figure 5.3, Table 5.1). As we have described in § 2.2, we failed to record the data to hard disks, but obtained the data via the telemetry in $\sim$ 12 events/second. The level flight lasted $\sim$ 8800 seconds (2.4 hours), thus we got $\sim$ 100000 events in total.

We analyzed cosmic-ray environment in our simulation in a following way. We first

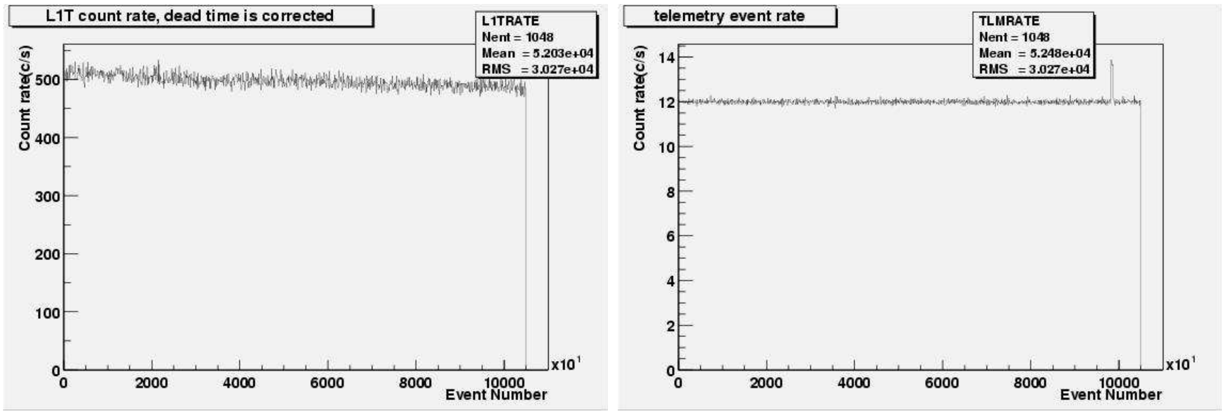

Figure 5.3: Level 1 trigger rate (Left) and telemetry event rate (right) during the level flight.

generated a particle of energy and direction based on a cosmic-ray model described in Chapter 4. We then constructed a sphere that contains whole pressure vessel (radius is 1.4 m) and took the disk that goes through the center of the sphere (an area is 6.18 m^2). A landing point of the particle is chosen randomly on the disk and finally the disk was rotated to be perpendicular to the direction of the particle. In this way, we can generate particles without distorting the original angular distribution. We generated about 1 million particles for each kind of cosmic-ray in the simulator and calculated corresponding exposure time based on the model flux and normalized the results to unit time. Below we compared the trigger rate and hit distributions in the TKR between the real data and simulation results for all events, charged events and neutral events.

All Triggered Events

We shot 783021 protons. The vertically downward flux is 327.96 counts/s/m^2/sr. Then the count rate of primary cosmic-ray proton at the disk is

$$327.96 \text{ counts/s/m}^2\text{/sr} \times 2\pi \text{ sr} \times 6.18 \text{ m}^2 = 12.7\text{k counts/s}.$$

The vertical flux of secondary proton is 70.66 counts/s/m^2/sr, then the count rate is

$$2 \times 70.66 \text{ counts/s/m}^2\text{/sr} \times 2\pi \text{ sr} \times (1 + \frac{3\pi}{20}) \times 6.18 \text{ m}^2 = 8.08\text{k counts/s}$$

for downward and upward secondary. Here the vertically downward flux is multiplied by $(1 + \frac{3\pi}{20})$ because the flux of secondary component has zenith angle dependence as $(1 + 0.6 \sin\theta)$, where θ is an angle from a zenith direction. Then the total count rate becomes 20.8k counts/s. Thus generated 783021 events correspond to 37.6 seconds in the real time. As for electrons, we shot 1 million particles and the vertical flux of primary component is 4.33 counts/s/m^2/sr. Then the count rate is

$$4.33 \text{ counts/s/m}^2\text{/sr} \times 2\pi \text{ sr} \times 6.18 \text{ m}^2 = 168.2 \text{ counts/s}.$$

Fluxes of secondary downward and upward electrons are 123.8 counts/s/m^2/sr and 121.7 counts/s/m^2/sr, respectively. Then count rate is

$$123.8 \text{ counts/s/m}^2\text{/sr} \times 2\pi \text{ sr} \times (1 + \frac{3\pi}{20}) \times 6.18 \text{ m}^2 = 7.08\text{k counts/s}$$

for downward, and

$$121.7 \text{ counts/s/m}^2\text{/sr} \times 2\pi \text{ sr} \times (1 + \frac{3\pi}{20}) \times 6.18 \text{ m}^2 = 6.95\text{k counts/s}$$

for upward electrons. Then the total count rate is 14.2k counts/s and 1 million electrons simulated correspond to 70.4 seconds. In the same way, total count rates of positron, $\mu^\pm$ and primary gamma-ray and secondary upward and downward gamma-ray are calculated as 8.34k counts/s, 4.00k/6.40k counts/s and 1.35k/44.9k/152k counts/s, respectively and the corresponding exposure becomes 120, 156/250, 740/22.3/6.58 seconds, respectively.

Next we calculated the trigger rate. As for protons, a number of triggered events is 8000 and a trigger rate becomes 212.5 Hz. Trigger rates of electron, positron, $\mu^\pm$ and gamma-ray are 80.2 Hz, 48.4 Hz, 54.3/32.6 Hz and 112.1 Hz, respectively. The total trigger rate is 540.1 Hz in simulation and is 8 % higher than that of the BFEM data. The trigger rate of each cosmic-ray is summarized in Table 5.2.

Finally we compared the TKR hit information. We extracted count rate of each SSDs layer for the BFEM data and the simulation and summarized the result in Figure 5.4. There the count rate of each SSDs layer of the balloon data and the simulation are shown in black and red line, respectively. In the balloon data, count rate gradually drops as layer number increases, whereas in the simulation a clear gap is seen between layer 15 and 16, and layer 17 and 18, corresponding to the boundary between incomplete/complete layers (Table 3.2) and a hump is seen around layers 10-15. Thus the distribution of them do not match. The contribution of each cosmic-ray type in the simulation is also shown in the right panel of Figure 5.4. There, proton, electron, positron, gamma-ray, μ^- and μ^+ are represented from bottom to top. The distribution of count rate of each SSDs layer of proton model, where primary is the dominant component, is similar to that of the BFEM data. On the other hand, other components, i.e., electron, positron, gamma-ray and $\mu^\pm$, show a hump around layer 10-15, and these particles are dominated by secondary components which have the angular dependence of the flux as $1 + 0.6 \sin\theta$. This facts may imply that the angular dependence of flux of secondary particles is not so strong as $1 + 0.6 \sin\theta$. The distribution of the number of hit SSDs layers in each event of the balloon data and the simulation, and the contribution of each particle type is shown in the left and right panel in Figure 5.5, respectively. We can see that the simulation overestimates the count rate for events which have relatively smaller number of hit layers. If particle has smaller energy or enters to the TKR from the side, then a number of hit layers becomes small. Thus we may need to modify the angular distribution or low-energy spectrum of cosmic-rays.

Charged Events

We next compared trigger rate for charged events. The number of charged events is 94445 and the trigger rate is 450 Hz in balloon data, and is well consistent with simulation results, 472.1 Hz, as shown in Table 5.2. In simulation data, charged events is dominated as 86.0 %

by charged particles. The count rates of each SSDs layer and the total number of hit layers of charged events are shown in Figure 5.6 and 5.7. As in the case of all events described above, simulation overestimates the count rate of each SSDs layer between layers 10-15, middle of TKR, and count rate of events which have 6-10 hit layers.

Neutral Events

About 10 % of obtained level flight data is classified as neutral events. Then, the number of events is 10374 and the trigger rate is 49.5 Hz. However the trigger rate in the simulation is 68.0 Hz, $\sim$ 40 % higher than the observed one as shown in Table 5.2. Count rates of each SSDs layer of neutral events of the balloon data and simulation are shown in the left panel of Figure 5.8 as a black and red line, respectively, and the contribution of each cosmic-ray type is shown in the right panel. Count rate in layers 0-5 are high in particular, because downward gamma-rays convert into e^-/e^+ pairs mainly at super GLAST lead (§ 3.2.2) placed under layer 6, 8 and 10, or most of upward going low energy particles are blocked by these lead. The simulation overestimates the count rate at almost all SSDs layer and failed to reproduce the "flat" distribution in layers 0-5 of the balloon data. A number of hit layers in an event is shown in Figure 5.9. The simulation again overestimates count rate of events where the number of hit layers is below 10. Since neutral events are mainly caused by gamma-ray, we might need to modify the flux of gamma-ray model to reduce these discrepancies.

We thus found discrepancies in count rate of each SSDs layer for charged events and trigger rate/count rate of each SSDs layer for neutral events. To solve these inconsistencies, and to obtain the reliable background model, we need to modify the simulator and/or generator. Since we have neglected materials outside the pressure vessel for simplicity, we first evaluate the effect of these materials in § 5.3. We then tune the cosmic-ray models up to solve the discrepancy. As we have examined above, the angular distribution of charged particles might be without $\sin\theta$ component (i.e., uniform distribution) and a flux of gamma-ray model might be smaller. Actually, angular distributions of secondary charged particles and gamma-rays are relatively uncertain (Chapter 4). We modify the angular distribution of gamma-rays (§ 5.4) and charged particles (§ 5.5) and examine how they solve the discrepancy.

Table 5.1: Trigger rate of each event type obtained by the BFEM.

All events	Charged events	Neutral events
500 Hz	450 Hz	49.5 Hz

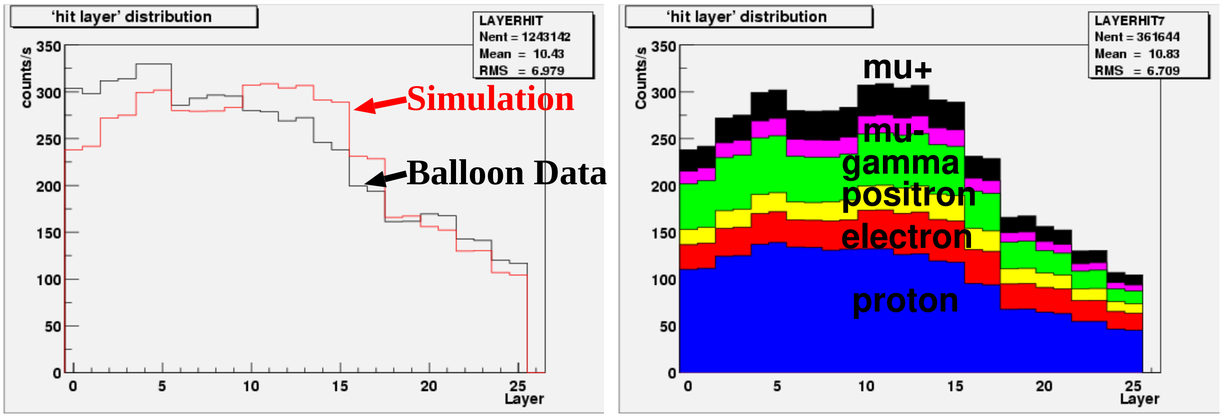

Figure 5.4: Count rate of each SSD layer for all events. The balloon data and the simulation result are shown in black and red line, respectively.

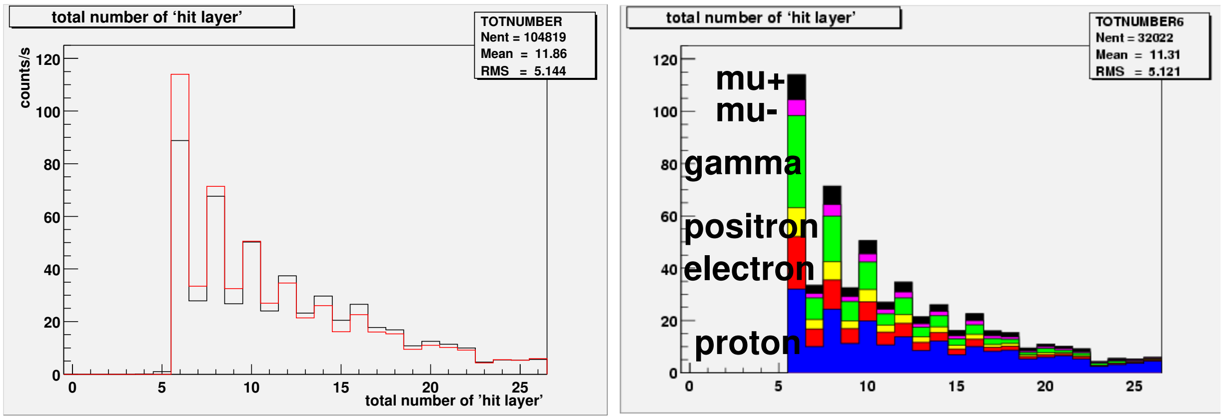

Figure 5.5: Number of hit layers in one trigger for all events.

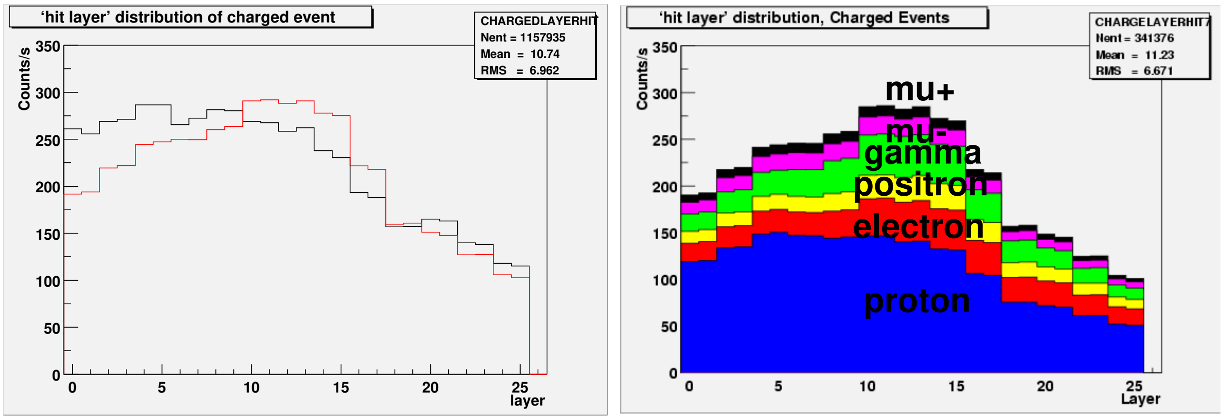

Figure 5.6: Count rate of each SSD layer for charged events.

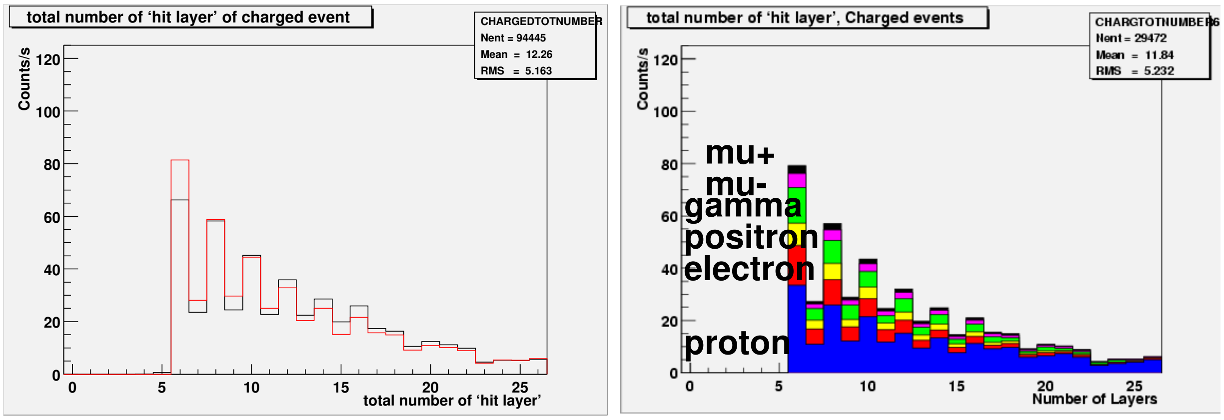

Figure 5.7: Number of hit layers in one trigger for charged events.

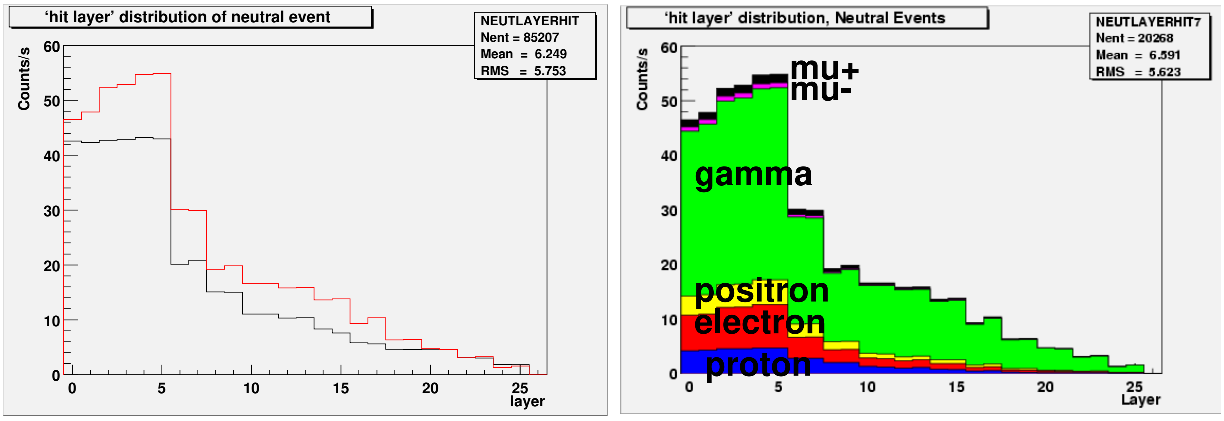

Figure 5.8: Count rate of each SSD layer for neutral events.

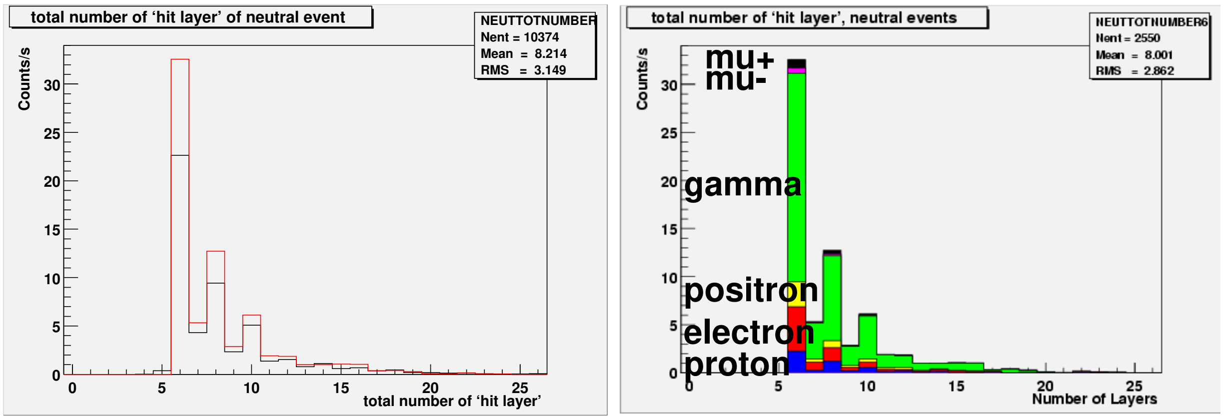

Figure 5.9: Number of hit layers in one trigger for neutral events.

Table 5.2: Trigger rate of each event type in the simulation. Contribution of each cosmic-ray component and total trigger rate are shown.

	proton	e^-/e^+	μ^-/μ^+	gamma	total
All events	212.5 Hz	80.2 Hz / 48.4 Hz	32.6 Hz / 54.3 Hz	112.1 Hz	540.1 Hz
Charged events	207.2 Hz	71.4 Hz / 43.4 Hz	31.6 Hz / 52.5 Hz	66.0 Hz	472.1 Hz
Neutral events	5.3 Hz	8.8 Hz / 5.0 Hz	1.0 Hz / 1.8 Hz	46.1 Hz	68.0 Hz

5.3 Effect of Materials Outside the PV

We have not implemented materials outside pressure vessel, e.g., gondola and batteries in the simulator for simplicity. These materials may block the cosmic-rays and influence both the trigger rate and count rate of each SSDs layer, thus we examined the effect of these materials here. The size of the gondola is about 2.45 m $\times$ 2.45 m $\times$ 4.04 m. Implementation of the gondola in the simulator is time-consuming because we need to enlarge the target area by a factor 3. Therefore we do not constructed the gondola in the simulator explicitly, but implemented effectively by adjusting the materials inside the pressure vessel. The mass and the size of the bottom part of the gondola is $\sim$100 kg and 2.45 m $\times$ 2.45 m, respectively. Since most of them are made of aluminum, the surface density becomes 1.67 g/cm^2. The mass of side structures of gondola and onboard batteries are $\sim$300 kg and most of them are placed around lower dome of the pressure vessel. We assumed the structure of those materials as an aluminum cylinder of 57 cm height, 119 cm radius and 5 cm thickness (1.448 g/cm^3). Most of these materials are placed in the direction of support structures when we look at them from the TKR, thus we implemented these materials effectively by increasing the thickness of support structures and keep target size small. We increased the thickness of lower cylinder plate by 6.19 mm (1.67 g/cm^2) to implement bottom structures of the gondola. As for side materials, a surface density is $\sim$7 g/cm^2 in a horizontal direction. In order to implement this structure, we increased the thickness of the middle cylinder by 3 cm corresponding to $\sim$7 g/cm^2.

With these new geometry described above, we ran the simulator again. No significant difference is recognized between trigger rate in new simulation results (Table 5.3) and that in the previous section (Table 5.2).

We also compared TKR hit information and collected them in Figures 5.10 to 5.13. No significant difference with the simulation results in the previous section is recognized again. A hump around layers 10-15 in a distribution of count rate of each SSDs layer is still exists for charged events (Figure 5.10), and simulation overestimates count rate of layers between 0-20 for neutral events (Figure 5.12) and count rate of events whose number of hit layers is relatively small (Figure 5.11 and 5.13). In short, the material outside the pressure vessel do not influence the trigger rate and TKR hit information very much.

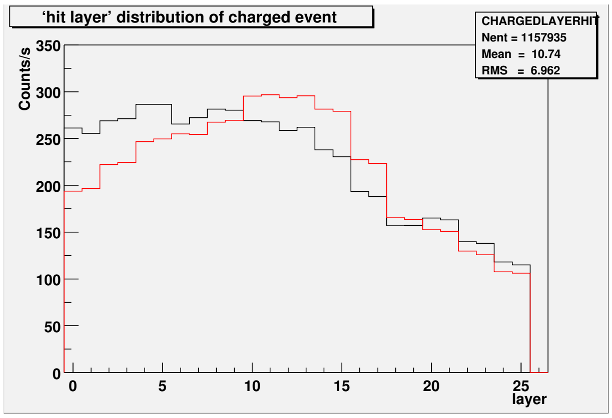

Figure 5.10: Count rate of each SSD layer for charged events. Materials outside the pressure vessel is taken into account.

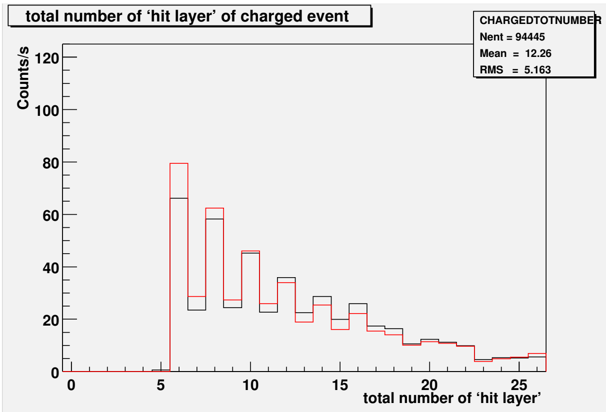

Figure 5.11: Number of hit layers in one trigger for charged events. Materials outside the pressure vessel is taken into account.

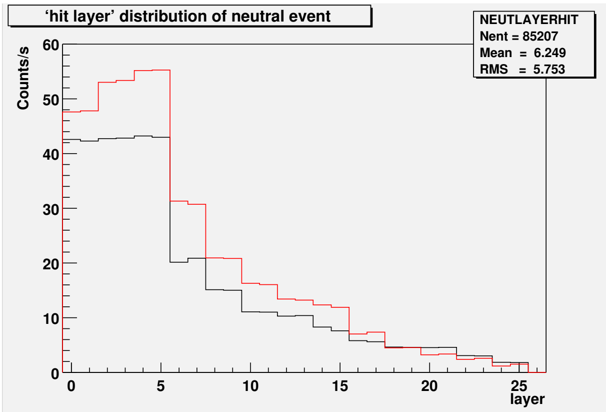

Figure 5.12: The same as Figure 5.10 but for neutral events.

Table 5.3: Trigger rate of each event type in simulation, where the materials outside the pressure vessel is taken into account effectively. Contribution of each cosmic-ray component and total trigger rate are shown.

	proton	e^-/e^+	μ^-/μ^+	gamma	total
All events	218.6 Hz	77.9 Hz / 46.2 Hz	32.8 Hz / 52.7 Hz	118.4 Hz	546.6 Hz
Charged events	213.5 Hz	69.8 Hz / 41.5 Hz	31.7 Hz / 51.3 Hz	71.1 Hz	479.5 Hz
Neutral events	5.1 Hz	8.1 Hz / 4.7 Hz	1.1 Hz / 1.4 Hz	47.3 Hz	67.7 Hz

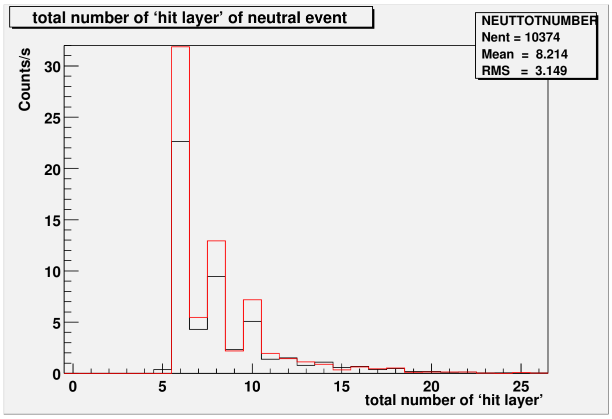

Figure 5.13: The same as Figure 5.11 but for neutral events.

5.4 Narrow Earth-rim Atmospheric Gamma Model

As we have discussed in § 5.2, Geant4 simulation overestimates the trigger rate and count rate of each SSDs layer for neutral events. Since neutral events are mostly gamma-ray origin and the measurement error of the angular dependence of atmospheric gamma-ray is relatively large (Figure 5.14), we have made peak width around 110 degree in the flux distribution narrower and see how the discrepancy is solved. The angular distribution of new model is shown in Figure 5.14 with the original one.

Then, the trigger rate becomes smaller especially for gamma-ray event, as given in Table 5.4. Trigger rates of both charged and neutral events are now consistent with that of the balloon data within 10 %.

The count rate of each SSDs layer and the number of hit layers for charged and neutral events are shown in Figure 5.15 to 5.18. Although the hump in layers 10-15 still exists for charged events (Figure 5.15), the count rates of each SSDs layer for neutral events decrease and shows good agreement between the balloon data and the simulation in layers 8-20, as shown in Figure 5.17. There still remain small discrepancy in layers 0-7 and above 20 and the simulation fail to reproduce the "flat" distribution in layer 0-5. The count rate in a distribution of the number of hit layers (Figure 5.16 and 5.18) decreased and agree with the balloon data better than the previous one (Figure 5.11 and 5.13), but the simulation still overestimates the neutral event rate where only 6 layers are hit by $\sim$ 20 %.

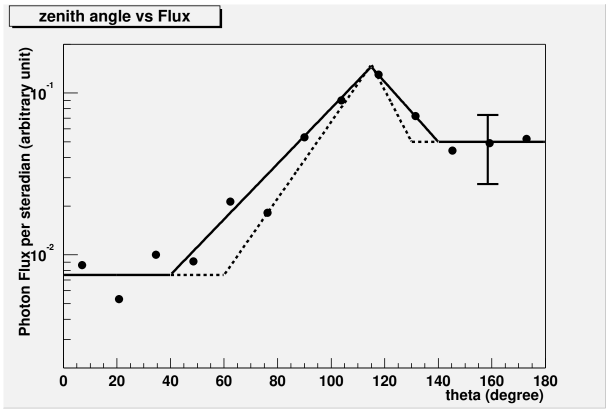

Figure 5.14: The revised model of gamma-ray angular distribution (dotted line) with the original one (solid line) and reference data (circles). A typical measurement error of the data is also shown.

In summary, trigger rate and count rates of each SSDs layer for neutral events in the balloon data are explained better with narrow earth-rim gamma-ray model. This fact may suggest peak width of zenith angle dependence of gamma-ray flux is narrower. However, there still remain discrepancy in a distribution of count rate of each SSDs layer for both charged events (layers 10-15) and neutral events (layers 0-5). We need to continue the examination to solve the discrepancy.

Table 5.4: Trigger rate of all events in simulation, where narrower-gamma model is applied. Contribution of each cosmic-ray component and total trigger rate are shown.

	proton	e^-/e^+	μ^-/μ^+	gamma	total
All events	218.6 Hz	77.9 Hz / 46.2 Hz	32.8 Hz / 52.7 Hz	89.2 Hz	517.4 Hz
Charged events	213.5 Hz	69.8 Hz / 41.5 Hz	31.7 Hz / 51.3 Hz	54.6 Hz	462.4 Hz
Neutral events	5.1 Hz	8.1 Hz / 4.7 Hz	1.1 Hz / 1.4 Hz	34.6 Hz	55.0 Hz

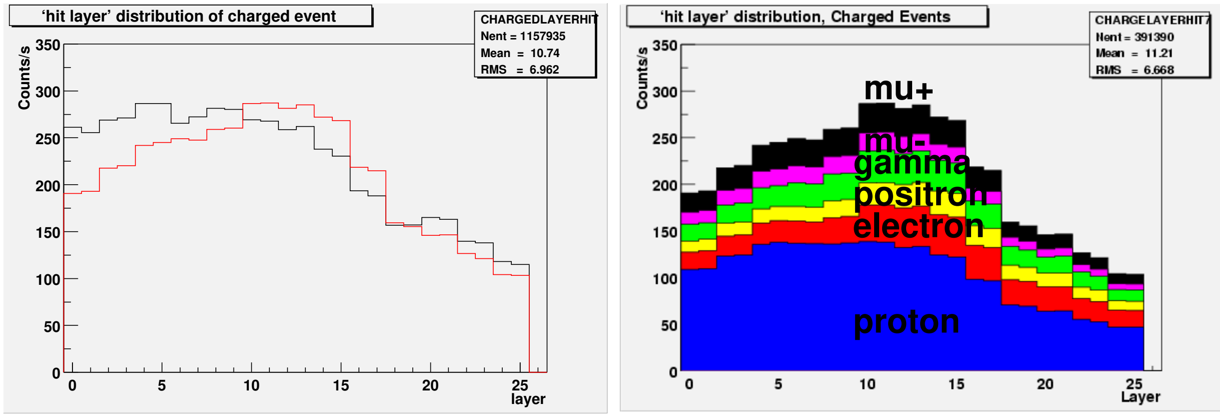

Figure 5.15: Count rate of each SSD layer for charged events, where narrower-gamma model is applied.

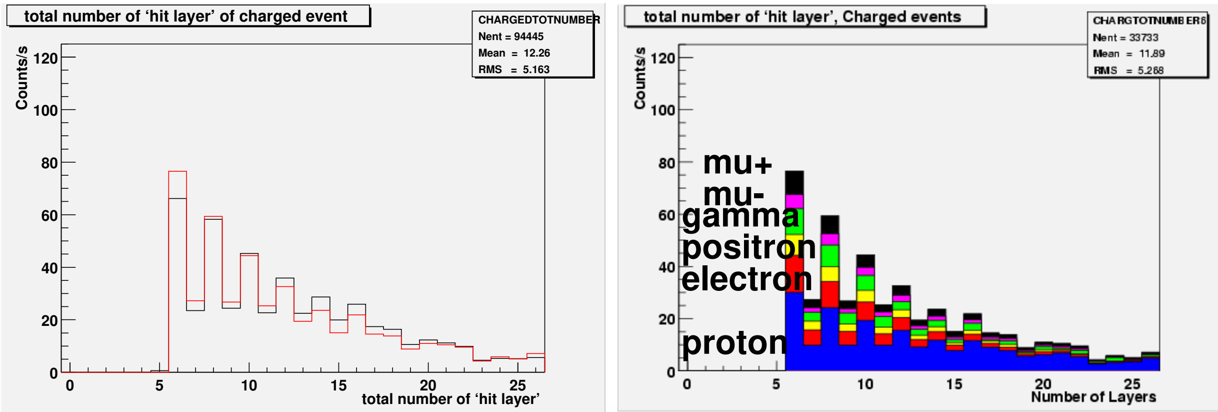

Figure 5.16: Number of hit layers in one trigger for charged events, where narrower-gamma model is applied.

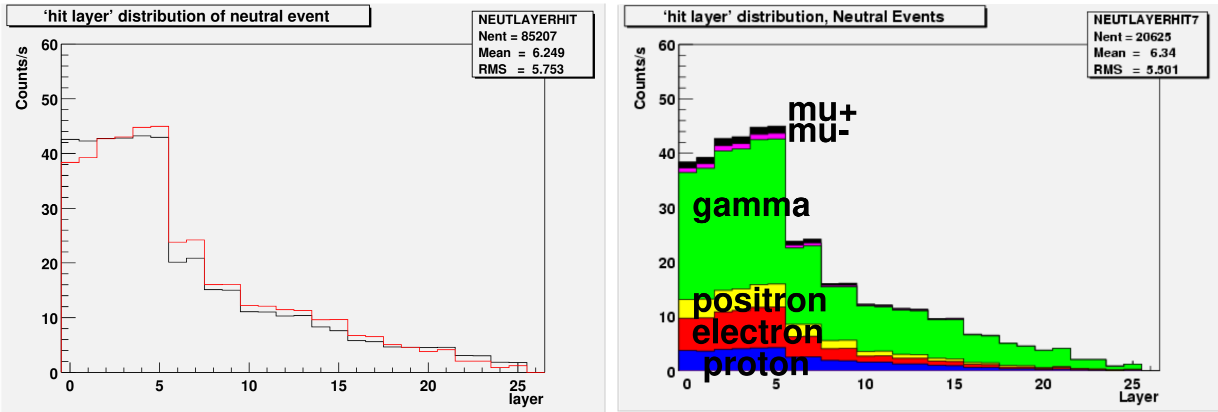

Figure 5.17: The same as Figure 5.15 but for neutral events.

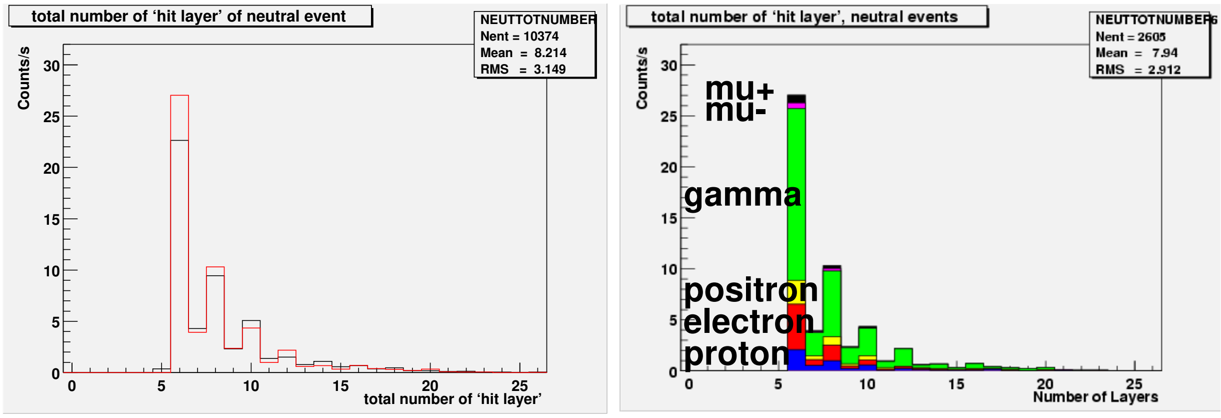

Figure 5.18: The same as Figure 5.16 but for neutral events.

.

5.5 Secondary Charged Particles with uniform angular distribution

In § 5.4, we examined trigger rate and count rate of each SSDs layer and distribution of the number of hit layers in an event with narrower angular distribution gamma-ray model, and trigger rate and count rate of each layer are well reproduced for neutral events. However, this model failed to explain some features of the balloon data, especially the count rate of each SSDs layer for charged events; although the simulation shows a "hump" around layers 10-15 in the distribution, the balloon data lacks such a structure and has relatively flat distribution around layers 0-15 (Figure 5.15). The hump is mainly produced by cosmic-ray electrons, positrons and muons, where the secondary component is dominant (§ 5.2). We therefore changed zenith-angle dependence of secondary charged particle fluxes into uniform and examined how it affects the trigger rate and the distribution of count rate of each SSDs layer and that of a number of hit layers, especially the count rates of each SSDs layer around layers 10-15 for charged events. A narrower earth-rim gamma-ray model, examined in the previous section, is used in this study.

The obtained trigger rates of all, charged and neutral events are collected in Table 5.5. A combination of narrower earth-rim gamma-ray model and uniform secondary charged particle cosmic-ray models reproduce the observed trigger rate within ∼10% for both charged and neutral events.

As for charged events, a "hump" around layers 10-15 in the distribution of count rate of SSD layers becomes less prominent, but the distribution between the balloon data and the simulation still differs with each other (Figure 5.19). The number of hit layers also show disagreement in event which have 8-20 hit layers (Figure 5.20). For neutral events, both the count rate and the number of hit layers in an event are better reproduced by our new models as shown in Figure 5.21 and 5.22. However, the simulation still fails to reproduce the "flat" distribution of count rate of each SSDs layer around layers 0-5 in the balloon data.

In short, even the combination of narrower gamma-rays model and charged particle cosmic-ray models of uniform secondaries cannot give us satisfactory results.

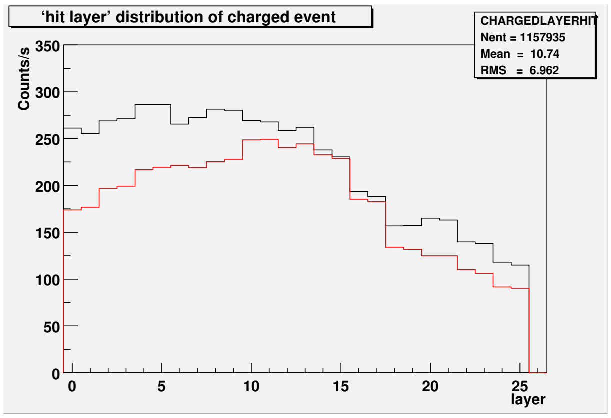

Figure 5.19: Count rate of each SSD layer for charged events, where the gamma-rays of narrower angular distribution and secondary charged particles of uniform distribution are utilized.

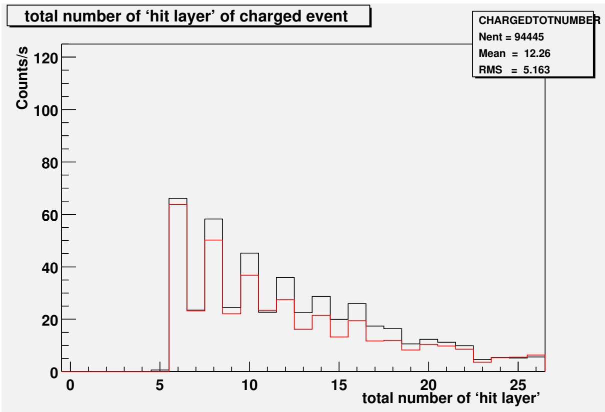

Figure 5.20: Number of hit layers in one trigger for charged events, where the gamma-rays of narrower angular distribution and secondary charged particles of uniform distribution are utilized.

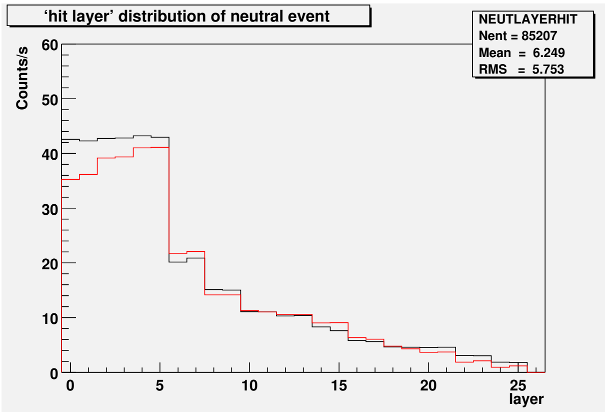

Figure 5.21: The same as Figure 5.19 but for neutral events.

Table 5.5: Trigger rate of each event type in the simulation, where the gamma-rays of narrower angular distribution and secondary charged particles of uniform distribution are utilized. Contribution of each cosmic-ray component and total trigger rate are shown.

	proton	e^-/e^+	μ^-/μ^+	gamma	total
All events	210.1 Hz	53.7 Hz / 32.2 Hz	22.7 Hz / 40.7 Hz	89.0 Hz	448.4 Hz
Charged events	205.5 Hz	48.5 Hz / 28.7 Hz	22.1 Hz / 38.8 Hz	54.6 Hz	398.2 Hz
Neutral events	4.6 Hz	5.2 Hz / 3.5 Hz	0.6 Hz / 1.9 Hz	34.4 Hz	50.2 Hz

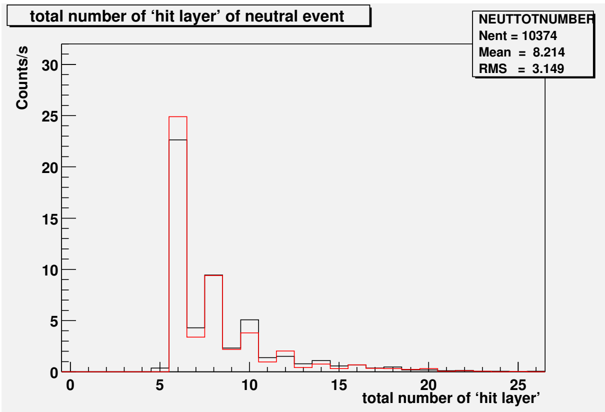

Figure 5.22: The same as Figure 5.20 but for neutral events.

5.6 BFEM Level 1 Trigger Condition

So far, we have compared the balloon data and simulation results, and faced several discrepancies. The major differences were as follows

1. Simulator overestimates trigger rate of neutral events.
2. In a distribution of count rate of each SSDs layer for charged events, a "hump" structure was recognized in the simulation results.
3. In the same distribution described above but for neutral events, simulation failed to reproduce the "flat" distribution around layers 0-5.

To solve these discrepancies, we made many attempts in the simulation, e.g., see the effect of materials outside the pressure vessel and modify the angular distribution of fluxes of secondary cosmic-ray particles where uncertainty of reference data is relatively large. Although the discrepancy 1 was relaxed by narrower earth-rim gamma-ray model, none of our attempts explain discrepancies of 2 and 3. This lead us to examine and investigate the balloon data itself instead of the geometry model and cosmic-ray generator.

The diagnostics of the trigger logic of the BFEM was done by T.Mizuno. The BFEM data contains layer number which cause the trigger in an event, and a distribution of the triggered SSDs layer is shown in Figure 5.23. In some unknown reason, layer 6, 14 and 15 do not contribute the trigger during the flight.

We thus took this into account and reprocessed our digitizer (TriggerFilterTkr.pl, § 3.4). Here, we used wide earth-rim gamma-ray model and charged cosmic-ray models with $\sin\theta$ component for secondary particles. The obtained trigger rate is collected in Table 5.6. Now, although the trigger rate for all and charged events are $\sim$ 15 % lower than that of the balloon data, trigger rate for neutral events is reproduced well.

We also compared TKR hit information as given in Figure 5.24 to 5.27. As for charged events, count rate of each SSDs layer in simulation dramatically decrease especially around layers 10-25, and well reproduced the balloon data (Figure 5.24). The simulation predicts lower count rate for all layers, and the difference of absolute count rate may be explained by implementing the heavy particle models (mostly He) and/or by modifying the flux of charged particle models whithin measurement error of the reference. As for neutral events, the “flat” distribution of count rate of each SSDs layer is also well reproduced in the simulation as shown in Figure 5.26. However, the count rate of layers 10-25 of the simulation now underestimates the balloon data. “Number of hit layers” for both charged and neutral events are still unsatisfactory (Figure 5.26 and 5.27).

In summary, we investigated the BFEM trigger condition and found that three layers do not participate to the trigger. We took this fact into account in our simulation, and succeeded to resolve the distinctive discrepancies of 1, 2 and 3. Trigger rates are reproduced within 15% for charged events and well reproduced for neutral events. The distribution of count rate of each SSDs layer are basically reproduced for both charged and neutral events. These results show our geometry and cosmic-ray models are basically good. In order to obtain a sufficient agreement between the balloon data and the simulation, however, we need to continue studying.

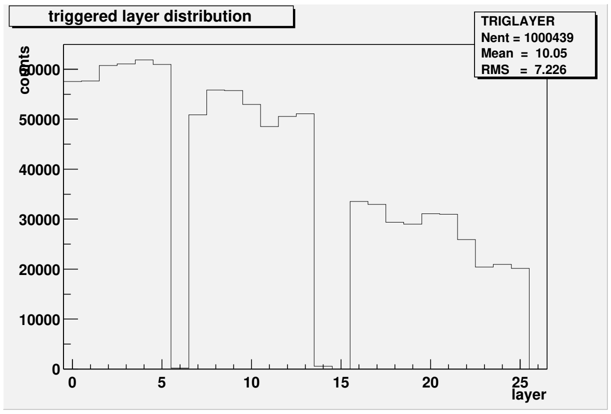

Figure 5.23: The number of contribution to trigger of each layer. It is found that layers 6, 14 and 15 hardly contribute to the trigger.

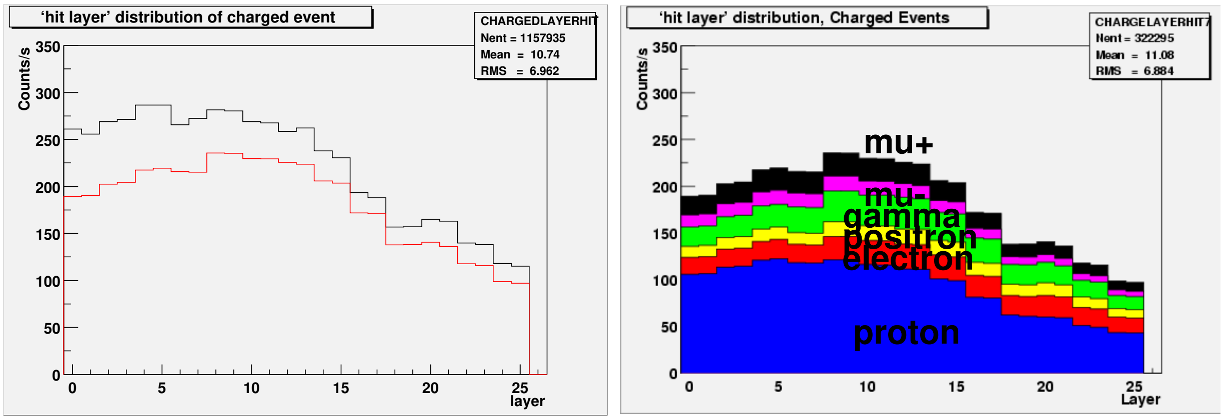

Figure 5.24: Count rate of each SSD layer for charged events, where layers 6, 14 and 15 are not used by the level 1 trigger.

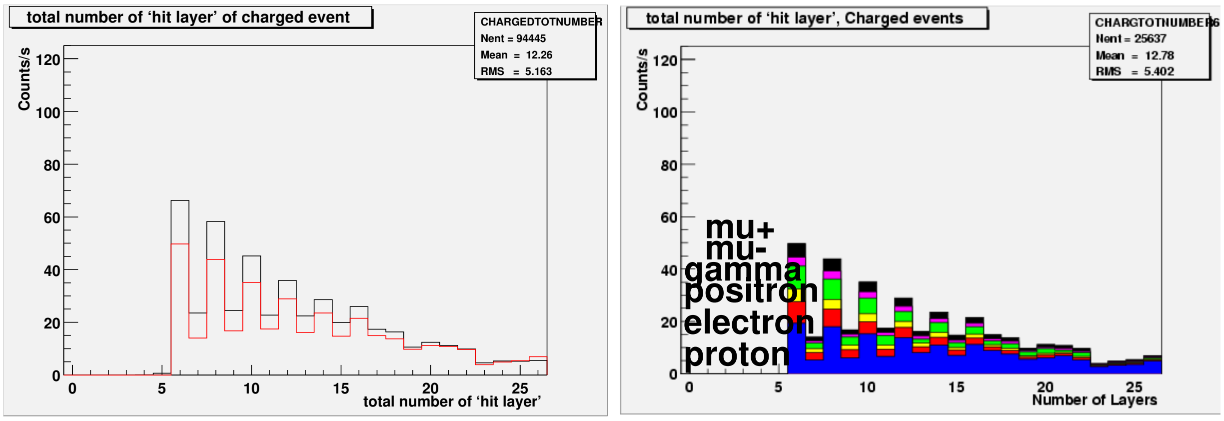

Figure 5.25: Number of hit layers in one trigger for charged events, where layers 6, 14 and 15 are not used by the level 1 trigger.

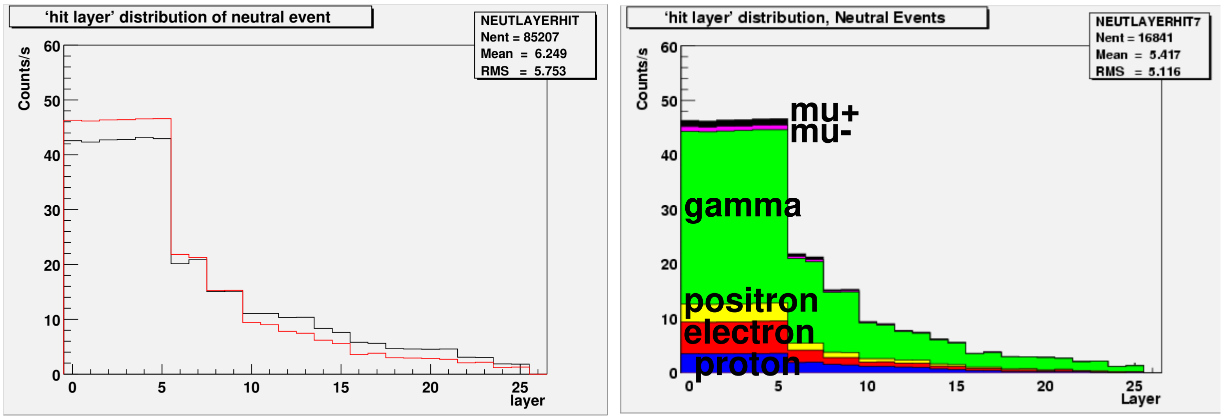

Figure 5.26: The same as Figure 5.24 but for neutral events.

Table 5.6: Trigger rate of all events in simulation, where layers 7, 14 and 15 are not used by the level 1 trigger. Contribution of each cosmic-ray component and total trigger rate are shown.

	proton	e^-/e^+	μ^-/μ^+	gamma	total
All events	179.9 Hz	55.5 Hz / 33.2 Hz	25.2 Hz / 40.0 Hz	91.3 Hz	425.1 Hz
Charged events	175.7 Hz	49.2 Hz / 29.6 Hz	24.3 Hz / 38.8 Hz	5.3 Hz	372.9 Hz
Neutral events	4.2 Hz	6.3 Hz / 3.6 Hz	0.9 Hz / 1.2 Hz	35.9 Hz	52.1 Hz

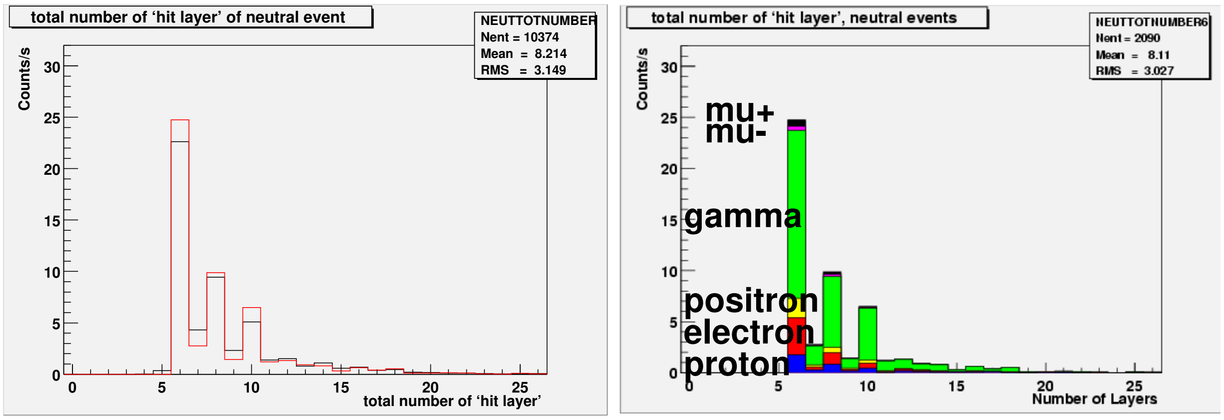

Figure 5.27: The same as Figure 5.25 but for neutral events.

Chapter 6

Conclusion

We have developed the GLAST balloon experiment simulator and cosmic-ray generators in order to study the radiation environment similar to that of the low-earth orbit. To obtain reliable cosmic-ray background models, we compared the simulation data with the balloon experiment data, in terms of trigger rate and TKR response. Some discrepancies were found between the balloon data and the simulation (§ 5.2), and we discussed geometry model and angular distribution of fluxes of cosmic-ray models. During the study, it was shown that the BFEM could constrain the angular distribution of secondary cosmic-rays (§ 5.4 , 5.5). We finally succeeded to resolve discrepancies by taking into account the BFEM trigger condition (§ 5.6), indicating that our simulator and generator are basically appropriate. In order to obtain firm results, however, we still need to continue studying, e.g., investigation of the real data, further tune-up of cosmic-ray models and development of other cosmic-ray model as heavy particles. We also plan to utilize the data of the XGT, the ACD and the CAL and compare the data and simulation throughly.

Acknowledgement

I would like to thank Prof. T.Ohsugi and Prof. T.Kamae for the supports on my study. I am grateful to Prof. Y.Fukazawa for the guidance. I wish to thank Dr. T.Mizuno for continuous counsel. I would like to acknowledge Dr. Y.Iwata and Dr. S.Yoshida for the advice. I thank to the GLAST balloon team. I thank also Mr. S.Ogata, Mr. H.Masuda, Mr. K.Yamanaka and all the members of the High-Energy Astrophysics and Particle Physics (Experiment) Laboratory.

Bibliography

[1] Eduardo do Couto e Silva, et al. Nuclear Instruments Methodd A, 471, 19-37, 2001

[2] K.Hirano, master thesis, Feb 2001.

[3] GLAST Testbeam Users guide, Jan 2000.

[4] R.P.Johnson, http://www-sldnt.slac.stanford.edu/glast/testbeam/TRK2000_003.doc, 2000.

[5] T.Handa, et.al., Digitization and Conversion Scripts for GLAST G4 Balloon Sim, Aug 2001.

[6] Y.Satou, bachelor thesis, Feb 2001.

[7] H.Mizushima, T.Mizuno, Validation of Geant4 Balloon Test Simulator (BalloonTestV13), Aug 2001.

[8] H.Mizushima, T.Mizuno, Validation of Geant4 Simulator for GLAST Balloon Test Flight, Aug 2001.

[9] L.J.Glesson, W.I.Axofrd, SOLAR MODULATION OF GALACTIC COSMIC RAYS, 1968, ApJ, **154**, 1011.

[10] Zombeck, Handbook of space astronomy and astrophysics, 2nd edition, Cambridge University Press, p. 225, 1990

[11] M.S.Longair, High Energy Astrophysics, 2nd edition, Cambridge University Press, pp. 325 330, 1992

[12] AMS Collaboration, Protons in near earth orbit, 2000, Physics Letters, **472**, 215.

[13] T.Sanuki et.al., Precise Measurement of Cosmic-Ray Proton and Helium Spectra with the BESS Spectrometer, astro-ph/0002481, 2000.

[14] J.A.Van Allen and A.V.Gangnes, The Cosmic-Ray Intensity Above the Atmosphere at the Geomagnetic Equator, Physical Review, **78**, 50, 1950.
On the Azimuthal Asymmetry of Cosmic-Ray Intensity above the Atmosphere at the Geomagnetic Equator, Physical Review **79**, (1950), 51.

[15] S.F.Singer, The Zenith Angle Dependence of the Cosmic Radiation above the Atmosphere at $\lambda = 41^\circ$ N, Physical Review, **77**, 729, 1950.

[16] Y.Komori, et.al., Proceeding of Dai-Kikyuu Symposium at ISAS, p33, 1999.

[17] J.Alcaraz et al. (AMS Collaboration) Leptons in near earth orbit, Phisics Letters, B484, 10, 2000.

[18] R.L.GOLDEN et al. MEASUREMENT FO THE POSITRON TO ELECTRON RATIO IN THE COSMIC RAYS ABOVE 5 GeV, ApJ, 457, 103, 1996.

[19] M.BOEZIO et al. THE COSMIC-RAY ELECTRON AND POSITRON SPECTRA MEASURED AT 1 AU DURING SOLAR MINIMUM ACTIVITY, ApJ, 532, 653, 2000.

[20] P.Sreekumar, et al. EGRET Observation of the Extragalactic Gamma Ray Emission, ApJ, 494, 523, 1998.

[21] V.Schönfelder, et al, The Vertical Component of 1-20 MeV Gamma Rays at Balloon Altitudes, ApJ, 240, 350, 1980.

[22] R.R.Daniel, et al, Gamma-Ray-Produced Electrons and Gamma Rays in the Atmosphere, Review of Geophysics and Space Physics, 12, 233, 1974.

[23] W.L.Imhof, et al. Measurements of Atmospheric Gamma Rays from a Satellite, Journal of geophysical Resarch, 81, 2835, 1976.

[24] Y.A.Kur'yan, et al, Investigation of the Hard Gamma Radiation of the Atmosphere on Kosmos 461, Geomagnetism and Aeronomy, 19, 6, 1979.

[25] J.M.Ryan, et al. Atmospheric Gamma Ray Angle and Energy Distribution, Journal of geophysical Resarch, 84, 5279, 1979.

[26] D.J.Thompson, A Three-Dimensional Study of 30 to 300 MeV Atmospheric Gamma Rays, Journal of geophysical Resarch, 217, 306, 1974.

[27] V.Schönfelder, et al. Diffuse Cosmic and Atmospheric MeV Gamma Radiation from Balloon Observations, ApJ, 217, 306, 1977.

[28] T.Mizuno, Count rate/Live time information of BFEM data, http://www.slac.stanford.edu/ mizuno/GLAST/Balloon/BalloonInfo2/Info.html.